Sedimentary processes and facies on a high-latitude passive continental margin, Wilkes Land, East Antarctica

Sandra Passchier[1]*, Daniel J. Ciarletta[1], Victor Henao[1], Vicky Sekkas[1]

[1]*Department of Earth and Environmental Studies, Montclair State University, Montclair, NJ 07043, U.S.A.*

**Corresponding author (e-mail: passchiers@mail.montclair.edu)*

Abstract: The impact of high latitude physical processes on the sedimentary geology of a passive continental margin is addressed here using a sediment record from the Wilkes Land margin of Antarctica. We present sequence stratigraphic models based on analytical data and genetic interpretations of sedimentary facies assemblages observed in drill cores collected by the Integrated Ocean Drilling Program (IODP). The examination of drillcores within a previously published seismostratigraphic context enhances the resolution of the sequence stratigraphic interpretations. At high latitudes, weaker tidal forcing, a stronger Coriolis effect, and more pronounced seasonality are some of the physical processes that impact erosion and sedimentation even if ice sheets are absent. Additionally, the presence of an ice sheet affects erosion rates, crustal motion, atmospheric and ocean circulation, with major implications for the development of depositional systems. As a result, high latitude, ice-covered, passive margins show distinct sedimentary facies associations and their interpretation requires the application of a different suite of sequence stratigraphic models than those applied to low-latitude continental margins.
End

High latitude passive continental margins with ice sheets are characterized by high sediment supply and strong, deflected bottom currents. A large temperature gradient caused by ice growth leads to strong katabatic wind fields that extend across the ocean and drive wind-driven contour currents (Goldner *et al.* 2014). Sea ice and polynya formation produces hypersaline shelf water on the continental shelf. A stronger Coriolis force at high latitude results in extreme deflections of surface currents and hyperpycnal flows, and as a result, an asymmetry of deep-sea levee systems (Peakall *et al.*, 2012; Wells & Cossu, 2013). Together, the large sediment supply and strong contour currents also provide increased potential for the development of sediment drift systems (e.g., Kuvaas & Leitchenkov 1992; Rebesco *et al.* 1996; Uenzelmann-Neben & Gohl, 2014).

Ice growth also gives rise to steric and glacio-isostatic effects that control continental shelf sedimentation and erosion (Boulton 1990; Stocchi *et al.* 2013). Upon ice growth to the edge of the continent, a moat develops on the continental shelf fringed by a forebulge in the off-shore direction. These geodynamic processes result in the development of depocenters on passive continental margins during glacial phases, trapping sediment on the continental shelf and starving the continental slope and rise. Upon ice retreat, continental shelves rebound, decreasing accommodation and resulting in sediment bypassing to the continental rise. In addition, the deglacial dissociation of gas hydrates that can form in shallower water on passive high latitude continental margins (Kvenvolden 1993) is also expected to promote erosion and sediment delivery to the deeper portions of the continental slope and rise (Paull *et al.* 1996; Maslin *et al.* 1998).

Here we investigate the role of these processes in the sequence stratigraphic interpretation of sediment cores collected on the Wilkes Land continental margin in Antarctica. This part of East Antarctica has developed a passive margin with a relatively narrow continental shelf. Following the break-up of Australia and Antarctica at ca. 83 Ma, a thin Eocene and older syn-rift sedimentary sequence was emplaced, overlain by thick Oligocene and younger post-rift sediments (Escutia *et al.* 2000; Close *et al.* 2009). The opening of ocean gateways in the middle Eocene (Kennett, 1977; Stickley *et al.*, 2004; Bijl *et al.* 2013) resulted in stepwise regional cooling, which possibly augmented by carbon cycle feedbacks resulted in the onset of continental-scale glaciation near the Eocene-Oligocene boundary (DeConto & Pollard 2003; Zachos *et al.* 2001, 2008; Passchier *et al.* 2017). Between 35 and 32 Ma the Tasman Gateway deepened, followed by the establishment of the Antarctic Circumpolar Current ~30 Ma as the Southern Hemisphere (SH) westerlies migrated across the Tasmanian Gateway (Stickley *et al.*, 2004; Scher *et al.* 2015).While the tectonic history of the Wilkes and Aurora subglacial basins can only be assessed remotely due to the presence of the East Antarctica Ice Sheet, the nearby Transantarctic Mountains show that uplift was relatively rapid with a maximum in denudation in the mid-late Eocene to Oligocene between ca. 43 and 26 Ma (Miller *et al.* 2010).

Two IODP drillholes at Sites U1356 and U1360 (Figure 1) recovered continental shelf and deepwater sedimentary strata spanning the Eocene to Miocene time of passive margin development and ice growth in East Antarctica (Escutia et al., 2011). The rotary core barrel (RCB) drilling system at IODP Site U1356 targeted the post-rift successions separated by four regional unconformities, WL-U3, WL-U4, WL-U5, and WL-U5b identified in multi-channel seismic reflection profiles (Escutia *et al.* 2000, 2005, 2011; De Santis *et al.*, 2003; Figure 2). IODP Site U1356 was drilled at 63°18.6138′S, 135°59.9376′E at 3992 meters below sea level (mbsl) at the transition between the continental rise and the abyssal plain and reached a depth of 1006.4 meters below the seafloor (mbsf) (Escutia *et al.* 2011; Figure 1). The paleolatitude of Site U1356 changed gradually from ~57°S to 59°S between 45 and 20 Ma and the Site started to move poleward more rapidly in the past 20 million years (Van Hinsbergen *et al.* 2015). Hole U1360A, sited approximately 65 kilometers off the Adélie Coast of East Antarctica on the Wilkes Land continental shelf was located in 495 meters of water and drilled to a depth of 70.8 mbsf (Figure 1).

Site U1356A is presently located landward of the Antarctic Polar Front in the area of the Antarctic Divergence. On Antarctica's distal continental rise currents dominate the sedimentary processes. Current speeds at the drillsite are controlled by the position of the Antarctic circumpolar currents relative to the drillsite and the intensity of wind-driven surface currents. Ninety percent of iceberg tracks for bergs larger than 5 m follow the eastward flowing Polar Current landward of Site U1356A and are expelled into the Southern Ocean from the Weddell Sea (Stuart & Long, 2011). Few icebergs pass over Site U1356 at this time.

The chronostratigraphic framework for U1356 (Tauxe *et al.* 2012; Bijl *et al.* 2013) shows that the strata encompass four relatively continuous sedimentary successions aged 54 Ma to present separated by hiatus or condensed intervals at 52-49 Ma, 42-34 Ma, 23-17 Ma, and 13-4 Ma, with high sedimentation rates at ~25-23 Ma and ~17-13 Ma. Unconformity WL-U3 (42-34 Ma) onlaps onto a structural high and strata above and below it are acoustically stratified (Figure 2). Based on the seismic architecture and internal acoustic facies properties, the strata between WL-U3 and WL-U4 were interpreted as distal turbidite, contourite, and hemipelagic deposits (Escutia *et al.* 2000). WL-U4 marks a shift from distal to more proximal deepwater deposits and separates acoustically stratified facies below from stacked channel levee and overbank deposits above. Unconformities WL-U5 and WL-U5b separate stacked channel levee from overbank deposits originating from two adjacent deep sea channels. Based on the multi-channel seismic data, levee deposition was interpreted to mark times when high volumes of sediment were delivered to the continental margin with wavy reflectors indicating reworking of turbidite deposits by bottom currents (Escutia *et al.* 2000, 2002; Donda *et al.* 2003) or compression due to slumping and other mass-wasting processes (Donda *et al.* 2008; Close 2010).

We interpret the sequence stratigraphy of the Wilkes Land margin using sedimentary facies analysis, laser particle size records, and bulk sediment geochemistry, from observations on the cores and integrate these with the broadscale seismic interpretation (following similar principles as outlined in Rijsdijk *et al.* 2005). Despite the absence of borehole geophysics shipboard scientists of IODP Expedition 318 were able to carry out broad scale correlations between seismic reflections and the lithostratigraphy and provided preliminary interpretations of depositional environments for each of the lithostratigraphic units (Escutia *et al.* 2011). Here we present sequence stratigraphic models based on extensive post-cruise sedimentological observations, analytical data, and genetic interpretations of the sedimentary facies assemblages. This type of high-resolution sequence stratigraphy is not possible using the seismic facies alone, because of the much lower resolution of seismic data in the depth domain. Our new genetic interpretation of the sedimentology, however, is discussed within the context of previous interpretations of the seismic data by others based on the description of the depositional systems in three dimensions (De Santis *et al.* 2003; Escutia *et al.* 2005, 2011).

MATERIALS AND METHODS

The lithostratigraphy of Holes U1356A and U1360A was described shipboard (Escutia *et al.* 2011) and post-cruise through macroscopic and smearslide observations. For gravel-bearing sediments the classification scheme of Moncrieff (1989) was used, whereas gravel-free sediments were classified according to Mazzullo *et al.* (1988). In these classification schemes, diamictites are sediments with gravel clast percentages 1-40 %, whereas conglomerates have gravel clast percentages > 40%. Sediments with a significant biogenic component were classified as “ooze” when the number of biogenic grains exceeded 50% of the total in smear slide counts. The suffixes “-rich” and “-bearing” were used where biogenic grains accounted for 25-50% and 10-25% of the total number of grains respectively. Gravel-sized clasts (>2 mm diameter) were counted on the cut face of the core in 10 cm core segments. For a statistically significant gravel count, however, the 10 cm segments constitute a sample size that is too small. For this paper gravel clast percentages were, therefore, normalized to number of clasts per meter recovered section length.

Particle size analyses

Samples were prepared using standard operating procedures outlined in Konert & Vandenberghe (1997). Samples were mechanically and chemically disaggregated through ultrasonic treatment and heating with 30% hydrogen peroxide and 10% HCl. Samples were dispersed through addition of sodium pyrophosphate and the solutions were heated to allow all dispersant to dissolve. A Malvern Mastersizer 2000 laser particle sizer was used to measure the grain-size distributions of the samples. Instrument settings were based on the recommendations of Sperazza *et al.* (2004). Industrial and natural standards were monitored for quality control.

Sand, silt, and clay percentages were calculated according to the Udden-Wentworth grain-size scale (Wentworth 1922). The Uniformity Coefficient is defined as D60/D10 in which D60 is the diameter greater than that of 60% of the particles, and D10 is the diameter greater than that of 10 % of the particles. The Uniformity Coefficient hence is a measure of the sorting of the sediment, with large numbers (>4) indicating poorly sorted sediment. The shape index is calculated by dividing the average Sauter diameter by the average specific surface area for the grains in the sample population. Samples from tills are generally elongate and angular and have high uniformity values and low shape index, whereas samples from eolian dune sand are rounded and spherical and have low uniformity and high shape index. Besides mode of sediment transport, however, mineralogy can also influence grain shape and these factors have been taken into account using shipboard smearslide data. Sortable silt was calculated by taking the average grain-size diameter of the silt fraction (McCave 2008), but it is interpreted only qualitatively as a current strength indicator because of the effects of ice-rafting on the grain-size distributions.

Major and trace elements

The major and trace element geochemistry of 97 samples was determined onboard the Joides Resolution using an inductively coupled plasma-atomic emission spectrophotometer (Escutia *et al.* 2011). An additional 12 samples were analyzed after the cruise at Montclair State University to bridge a gap in shipboard sample collection through the Middle Miocene section. The shipboard and Montclair State University geochemistry labs used identical sample preparation procedures described in Murray *et al.* (2000). Circa 0.1 g of finely powdered sample was combined with 0.4 g of lithium metaborate and transferred to graphite crucibles for fusion in a furnace at 1050º C. The pellets were dissolved in diluted nitric acid of trace metal grade. At Montclair State University, solutions are measured in a Jobin-Yvon ULTIMA C inductively coupled plasma optical emission spectrometer (ICP-OES). Eleven USGS rock standards were also prepared and the results were used for elemental calibration. Typical errors are 3-5% for most elements except for P, which typically displays errors of 5-20%.

Ba-excess refers to the Ba concentration above detrital (lithogenic) input and is used as a proxy for marine barite ($BaSO_4$) concentration (Schenau et al., 2001). Si-excess is the SiO_2 concentration above lithogenic SiO_2 input and in deep-marine sediments is interpreted as a proxy for biogenic silica content (Böning et al. 2005). Lithogenic Ba-and Si contents were estimated from a mixing model constrained by the Ti/Al ratios using the average composition of clasts dredged from the seafloor near Mertz Glacier (Goodge & Fanning, 2010) and the average composition of Neogene diamicts from the Ross Sea continental shelf (Martin & Passchier, 2010, Hansen 2011).

RESULTS AND DISCUSSION

Barium and silicon excess

Ti/Al ratios are relatively stable throughout the hole, suggesting that long-term changes in provenance were not a major control on the bulk geochemistry. Ba-excess and Si-excess was calculated for the deep-marine continental margin sediments only (Paytan & Griffith 2007). Ba-excess mimics lithological changes (Figure 3) and is low in pinstripe laminated intervals of contourite facies assemblages and typically below 200 ppm in intervals of core with gravel-sized clasts.

Si-excess correlates well with the presence of diatomaceous or carbonate-bearing sediment and shows peak values exceeding 20 wt. % in several intervals with gravel sized clasts. Si-excess does not correlate to Ba-excess, suggesting that changes in silica availability and bottom oxygen conditions played a role in their distribution. Ba-excess is low where pyrite occurs, which suggests that the down hole distribution of Ba-excess is influenced by bottom oxygen conditions, besides productivity. The down hole distribution of Si-excess is not the result of dilution by variations in terrigenous sedimentation, because the highest Si-excess values are found in intervals with the highest terrigenous sedimentation rates.

Studies of modern sediment traps show a strong correlation between diatom productivity and benthic fluxes (Pondaven *et al.* 2000), and if this correlation is also valid in the past, the peaks in Si-excess concentrations can be interpreted as diatom productivity events. Under the present interglacial conditions the maximum diatom productivity is found just south of the Polar Front

Zone in the Southern Ocean, an area underlain by sediments with high concentrations of biogenic silica, also known as the opal belt (Zielinski & Gersonde 1997; Pondaven *et al.* 2000; Anderson *et al.* 2009). For the most recent glacial cycle, Si-productivity appears to be controlled by upwelling intensity from deep waters that are enriched in dissolved silica (Anderson *et al.* 2009). These upwelling deep waters are also oxygen depleted, and it could explain the low Ba-excess values in intervals of high Si-excess. The upwelling intensity in the Southern Ocean coincides with Antarctic warm events and deglaciation and appears to be controlled in part by the strength and position of the SH westerlies around the latitude of the Drake Passage, although the exact mechanisms are poorly understood (Toggweiler *et al.* 2006; Anderson *et al.* 2009).

The down core variations in particle size distributions for Site U1356 are presented in Figure 4. Based on the particle size distributions seven major stratigraphic units (labeled A through G) can be distinguished that can be tied to seismostratigraphic units (Escutia *et al.* 2011). Representative core sections and particle size distributions for each facies are displayed in Figures 5-9. The age model applied here is from Tauxe *et al.* (2012). For the Eocene section, a more detailed graphic log was created (Figure 5).

Early to mid-Eocene continental shelf environments

Site U1356 - Unit A (948-1006 mbsf): early Eocene mid-shelf (54-52 Ma)

The early Eocene strata drilled at Site U1356 consist of stratified dark green bioturbated siltstone (Figures 5, 6, Unit A). Cm-scale bedding is observed, and ripple-laminated sandstone interbeds are present, as well as one texturally immature subarkose interbed (~982 mbsf). A *Zoophycos* ichnofacies is present throughout and pyrite is a common sediment constituent (Expedition 318 Scientists 2011a). The particle size distributions show evidence of very high silt percentages and grain shapes are spherical. The sediments are extremely well sorted (Figure 4).

The dark green bioturbated siltstones (Figure 6, Unit A) were likely deposited below wave base. The presence of very well-sorted silt with spherical grain shapes (Figure 5, Unit A) is consistent with a fluvial suspended sediment input into a shallow marine environment. A *Zoophycos* ichnofacies in the dark green claystones is indicative of low oxygen values, also pointing to a lack of wave stirring and a stratified water column. This facies shows similarities to those attributed to a mid-shelfal prodelta depositional environment in the low-latitude Upper Cretaceous coastal plain in New Jersey (Owens & Sohl 1969; Miller *et al.* 2004), which also developed as a young passive margin sequence. The paleontological evidence is consistent with a mid-shelfal paleoenvironment for these strata drilled at Site U1356 (Pross *et al.* 2012; Bijl *et al.* 2013).

The early Eocene Wilkes Land hinterland was covered in tropical and subtropical forests along its coast and in coastal uplands (Pross *et al.* 2012). Clay minerals in the early Eocene mudstones are predominantly kaolinite (Houben *et al.* 2013) and both chemical weathering ratios (Passchier *et al.* 2013) and clay minerals suggest that the climate was humid and that unstable minerals were altered. The presence of a < 1 m thick bed of subarkose at ~982 mbsf, however, poses a challenge because of the low potential of survival of unstable minerals such as feldspars under humid conditions. The presence of texturally immature subarkose offshore cratons in tropical to subtropical regions has previously been explained in two ways (Damuth & Fairbridge 1970): 1) the continental conditions briefly turned arid or semiarid allowing feldspars to survive at the Earth surface even in near-ocean settings; or 2) near-shore uplift produced so much fresh rock material that chemical weathering was outpaced by rapid sediment transport and deposition. Between Australia and Antarctica, Eocene successions occur as drapes in the upper sections of rift basins associated with the extension-dominated segment between Wilkes Land and the Great Australian Bight. Directly to the East, however, are the transpressional fracture zones of the Oates Land-Tasman Rise segment, which extend back to the Paleocene/Eocene (Roehl *et al.* 2004; De Santis *et al.* 2010). A brief aridification of the Early Eocene Antarctic climate is not as plausible. Current available pollen records in Site U1356 (Pross *et al.* 2012) and dust fluxes to the southern Pacific Ocean (Dunlea *et al.* 2015) do not show evidence of aridification until the middle Eocene.

Site U1356 - Unit B (895-948 mbsf): middle Eocene inner shelf

The middle Eocene sediments consist of cross-bedded and planar bedded sandstone, diamictites, silty claystones, siltstones, and intraclast conglomerates with graded bedding and parallel lamination (Expedition 318 Scientists 2011a). Contorted bedding is occasionally present in the rock clast-bearing sandstones and diamictites between 942 and 927 mbsf, but the overlying fining-upward and rarely coarsening-upward beds between 919 and 896 mbsf are stratigraphically intact and contain mica, and locally glauconite and pyritized shell fragments (Figure 5). The fining upward beds between 919 and 896 mbsf contain thick basal units with numerous rounded sedimentary intraclasts capped by stratified silty sandstones and mudstones (Figure 6, Unit B). The rock clast-bearing units below 927 mbsf are separated from the graded sedimentary deposits by interbedded reddish brown clayey siltstones and laminated greenish gray and brown sandy mudstones between 927 and 919 mbsf.

The high sand percent together with high sortable silt values, low clay contents, and sediment sorting (Figure 4, Unit B) point to current influence on the sediments. The low shape index in this case is most likely the effect of the presence of the variable quantities of mica and glauconite, which are phyllosilicates with platy grain shapes.

The mid-Eocene strata represent a shallower depositional environment than the underlying Lower Eocene strata. The facies assemblages show greater variability which is more typical of inner shelf environments and sequences show similarities to more recent examples recorded in Pleistocene to Holocene drillcores from the New Jersey continental shelf (McHugh *et al.* 2010). The contorted clast-bearing sandstones and diamictites between 942 and 927 mbsf likely originated within shelf canyons or on lowstand delta top surfaces. The overlying interbedded reddish brown clayey siltstones and laminated greenish gray and brown sandy mudstones between 927 and 919 mbsf are more typical of tidally influenced restricted basins, sheltered from wave action, or lagoonal deposits (McHugh *et al.* 2010). During deposition of this facies the paleoshoreline was seaward of the drillsite. In contrast, the overlying fining-upward beds with thick basal beds of intraclasts indicate a waning flow regime, consistent with either a (storm) wave–influenced environment or a hybrid turbidity current – debris flow regime in a deeper sloping environment (McHugh *et al.* 2002; Shanmugan 2006; Hodgson 2009; Haughton *et al.* 2009). This facies, however, is rare in passive margin slope settings (McHugh *et al.* 2002) and the overlying sandy lithofacies, which include glauconite, shell fragments, and planar bedded cross-bedded sandstones (Figure 6, Section 95R4), are more typical of transgressive wave-dominated coastal sequences (Cleveringa 2000; Passchier & Kleinhans 2005; McHugh *et al.* 2010). In summary: the Middle Eocene strata likely represent a regressive, followed by a transgressive coastal system.

A shallower mid-Eocene depositional environment suggests that sediment supply exceeded post-rift subsidence. The shoaling would require an increase in continental erosion in the mid-Eocene. The mid-Eocene marks the onset of rapid uplift in the nearby Transantarctic Mountains (Miller *et al.* 2010), and such an event would result in higher denudation rates and sediment supply to the Wilkes interior basin, which forms the hinterland for the sedimentation at Site U1356. Evidence from dust fluxes to the South Pacific originating in Australia and perhaps also Antarctica also indicate the onset of a period of aridification around ~50 Ma (Dunlea *et al.* 2015). This early aridification, however, is not as evident in the Antarctic terrestrial palynology from this core (Pross *et al.* 2012).

Lowermost Oligocene glacially influenced continental shelf

Site U1360

At Site U1360 on the continental shelf of Wilkes Land, early Oligocene strata were recovered in Cores 2R-6R (14.3-53.8 mbsf)(Expedition 318 Scientists 2011b). Sandy diamict and stratified gravelly sand with traces of ripple cross-stratification in multiple directions and distinct back-filled burrows are found in a fining up sequence at the base (Figure 7, Section 6R1). These strata are overlain by rather homogeneous greenish or olive grey bioturbated sandy mudstones with dispersed outsized clasts (Cores 3R-5R, Figure 7). The strata contain common pyritized bivalve shell fragments and some pyritized diatoms. The sequence is capped with a greenish bioturbated claystone at the top of this truncated lower Oligocene section (2R-3R).

The fining up sequence is indicative of a deepening of the depositional environment (Houben *et al.* 2013). The coarse-grained cross-stratified sands with shell fragments and back-filled burrows in Core 6R show similarities to coarse-grained shoreface sands that have been described from transgressive coastal sequences and were deposited in a combined flow regime (Passchier & Kleinhans 2005). In contrast, the overlying mudstones with outsized gravel clasts (> 2 mm) were deposited below wave base. The presence of dispersed clasts in the mudstones suggests that sea surface temperatures were cold enough for floating ice to be present, which is also in agreement with the occurrence of dinoflagellate assemblages with sea-ice affinities (Houben *et al.* 2013).

Oligocene-Miocene glacially influenced deepwater depositional environments

Site U1356 Unit C: Lowermost Oligocene (862-895 mbsf)

Lower Oligocene strata of Unit C unconformably overly Middle Eocene strata of Unit B (Figure 5). The core section with the hiatus between Middle Eocene and Early Oligocene strata is visible in Figure 6 (Section 95R3-91 cm). The earliest Oligocene sediments drilled at Site U1356 (93R-95R) are characterized as contorted and convoluted massive and stratified sandy mudstones with dispersed gravel-sized clasts and light green laminated claystones (Figure 8D, E). Above the coarse-grained beds are ripple cross-laminated sandstones with glauconite and massive, heavily bioturbated, dark brown and dark green silty claystones and clayey siltstones (Figure 6, Unit C), The claystones at the top of Unit C contain abundant pyrite and dm-scale calcareous interbeds are noted.

The particle size distributions of the sediments in Unit C is variable with a significant clay and silt component and the presence of sand and gravel (Figure 4). Some intervals are extremely poorly sorted with very low grain shape index, in this context, most likely indicative of a glacial origin for the sediment.

The contorted and convoluted beds with coarse fraction at the base of the sequence probably represent glaciomarine sediments with IRD, which have been affected by local slumping. These sediments were not transported far and preserve some of their original structure. This interval dates to about 33.6-33.2 Ma contains dinoflagellate assemblages with sea-ice affinities (Houben *et al.* 2013). In the early Oligocene Site U1356 was opposite the west Tasman Rise near the continent-ocean boundary of East Antarctica (Scher *et al.* 2015). Between 35 and 32 Ma the west Tasman rise deepened from less than 400m to bathyal depth (Stickley *et al.* 2004) and it is possible that the Antarctic continental rise near Site U1356 was affected by active tectonics as well. The planar-laminated and ripple-cross laminated sandstones with glauconite around 878 mbsf, may signal gravity flows bringing sand from the adjacent continental shelf. As mass flows ceased, pelagic sedimentation dominated and sediments became strongly bioturbated (Figure 3), however, with bottom conditions periodically becoming less oxygenated, as indicated by the presence of pyrite (Expedition 318 Scientists 2011a).

Site U1356 Unit D: Early-mid Oligocene (594-862 mbsf) – distal submarine fan

The strata between unconformities U3 and U4 have a sheet-like geometry with low-amplitude parallel internal reflectors. These strata were previously interpreted as a distal submarine fan (Escutia *et al.* 2000; 2005). Cores 64R-89R (Unit D) are dominated by strongly cyclical m-scale interbedded laminated and bioturbated cherty claystones with few gravel-sized clasts (Figure 4). Sharp-based, parallel and pinstripe laminated claystones (Figure 8A) and silty claystones (Figure 8C) have gradational upper contacts with overlying bioturbated claystones (Figure 8B). Isolated dm-scale interbeds of calcareous shale and clay-rich nannofossil ooze are also present. Dm-scale beds of ripple cross-laminated siltstone and sandstone are present between ~670 and ~680 mbsf and at ~845 mbsf (Figure 8B). These beds display lenticular bedding. Interbeds of sandy mudstones, which contain both rock and intraclasts and display horizontal shearing and contorted bedding are found at ~694-723 mbsf and convolute bedding with possible repetition of beds is found at ~783-832 mbsf (Expedition 318 Scientists 2011a).

The particle size distributions of the sediments are characterized with low sand percentages (< 10%) and highly variable silt and clay percentages associated with the cyclical facies transitions (Figure 4, Unit D). Silt percentages vary between 33 and 82%. Calcareous shale and nannofossil oozes are rich in clay (62-72% clay).

The localized ripple cross-laminated sandstone interbeds between ~670 and ~680 mbsf and at ~845 mbsf in Site U1356 (Figure 8B) represent enhanced bottom current activity, whereas the contorted sandy mudstones with gravel clasts at ~710-724 mbsf, and ~817-832 mbsf (Figure 8C), likely represent hemipelagic sediments with minor episodes of ice rafting between ~33 and ~26 Ma. Ice rafting marks the onset of ice retreat phases followed by glacio-isostatic rebound that periodically decreased accommodation on the continental shelf. The remarkable paucity of ice rafted debris in most of the Early-mid Oligocene section, however, suggests that high sea surface temperatures prevented iceberg survival, considering that the paleolatitude of Site U1356 was ~58°S around this time and near the northern edge of the polar front zone. The ripple cross-laminated sandstones could be related to the intermittent onset of strong wind-driven currents through the nearby Tasman Gateway around 30-29 Ma (Scher *et al.* 2015).

Site U1356 Unit E: Late Oligocene (442-594 mbsf) – stacked channel levee, proximal fan

In the seismic stratigraphy, the high amplitude stratification between unconformity U4 and U5 appears to delineate crudely bedded stacked channel levee deposits (Figure 2)(Escutia *et al.* 2005). The drilled succession in Cores 47R-63R, however, consists of interbedded calcareous shale and clay-rich nannofossil ooze, silty claystones with dispersed clasts and diamictites with intraclasts and contorted and sheared bedding (Figure 9E) (Expedition 318 Scientists 2011a). A few massive sand beds are also present. Thin dm-scale graded sand beds with partial Bouma bed structure are found at ~480 and ~536 mbsf, near the base of intervals with diamictites. Volcanic ash was noted in a smearslide of a bioturbated claystone with silt ripples at ~546 mbsf.

The particle size distributions in this interval are characterized with low clay percentages, extremely high silt/clay ratios and high sand percentages. A few sediments in the upper portion of Unit E (Figure 4) are poorly sorted with elongate grain shapes, consistent with a glacial influence on the sediments. This interval is also characterized with maxima in Si-excess, marking productivity events (Figure 4).

The sediments rich in biogenic material are interpreted as pelagic and hemipelagic. The high silt-clay percentages, however, are consistent with an episodic high terrigenous sediment supply, which overpowered the background fine-grained marine sedimentation. Rare claystones with gravel clast clusters are indicative of ice rafted debris (IRD; Bennett *et al.* 1996; Licht *et al.* 1999; Kilfeather *et al.* 2010), whereas the thick diamictites with intraclasts (Figure 9E) and horizontal and rotational shear structures are characteristic of debris flow facies (McHugh *et al.* 2002; Passchier *et al.* 2003). The massive sandstones could also be debrites and such deposits have previously been described from deep-marine Antarctic debris flow environments (Wright & Anderson 1982; Passchier *et al.* 2003).

The deposition of the nannofossil ooze interbeds in the late Oligocene requires a deep calcite compensation depth (CCD). The presence of nannofossil ooze further suggests that SST were periodically > 3-8 C, because nannofossil ooze is currently only deposited north of the Subantarctic Front (Whitehead & Bohaty 2003 and references therein). It is interpreted that nannofossil ooze deposition is associated with landward migration of the Antarctic Front and ice retreat. Nannofossil oozes are interbedded with sandy debrites that occur in seismic facies with channel levee geometries (Escutia et al., 2011)(Figure 2). The Upper Oligocene strata contain two extensive clast-rich intervals (at ~24 and 27 Ma), which occur in the sandy debrites.

The sandy debris flow events likely correspond to times when the Antarctic ice sheet retreated from the continental shelf. Consequently, glacio-isostatic rebound decreased accommodation on the continental shelf and allowed more sediment to bypass the shelf (cf. Boulton, 1990). Considering that the sands occur in stacked channel levees, it becomes likely that the sands represent levee collapse events during times of flow in the channel. As the channels increase in elevation over time, they become too high for flow to overtop the levees, and the levees become prone to collapse. Gravity flow as a result of gas hydrate instability (Paull *et al.* 1996; Maslin *et al.* 1998) due to ocean warming may have played a role in these Oligocene events. Alternatively, sea floor instabilities related to volcanic and seismic activity may have contributed to the instability as evidenced by the presence of volcanic ash at ~546 mbsf (Expedition 318 Scientists 2011a).

Site U1356 Unit F: Early Miocene (278-442 mbsf) – distal channel levee with sediment waves

The seismic stratigraphy above unconformity U5 is characterized by high amplitude wavy stratification and is interpreted as distal channel levee deposits with sediment waves (Escutia *et* *al.* 2005). This interval at 278-442 mbsf (Cores 30R-47R) is characterized by diatomaceous and cherty clayey siltstones (Figure 3). A facies association of m-scale interbedded bioturbated (Figure 9D) and pinstripe laminated (Figure 9C) claystones can be observed, but bioturbation is common in both sub-facies (Expedition 318 Scientists 2011a). One dm-scale fining up sandstone bed with rip-up clasts at its base and planar lamination on top was observed at 329 mbsf (Figure 35R-3). Other ripple cross-laminated sand beds are also present. However, none of these sand beds are graded or display a clear Bouma bed structure. Outsized clasts are extremely rare and were only found in current bedding at ~329 and ~383 mbsf. A ca. 6-million year hiatus (~23-17 Ma) is present above 432 mbsf (Tauxe *et al.* 2012) and may be attributed to multiple episodes of erosion or non-deposition.

The particle size distributions of these sediments (Figure 4) are quite uniform in character with high silt content (64-81%), generally <10 % sand with an absence of sand ~400-430 mbsf (3 samples). The sediments are generally well-sorted and particle shapes have some sphericity (shape index 0.2-0.3), except for the intervals with the gravel sized clasts near ~329 and ~383 mbsf, which also have the highest sand percentages.

Strong bottom currents could have contributed to the origin of the hiatus dated ~23-17 Ma (Tauxe *et al.* 2012) near the base of this Unit. The interval between ~23 and 17 Ma is recognized in previous studies as a period of intensification of the ACC resulting from an increasing depth and widening of the Drake Passage (Lyle *et al.* 2007). Furthermore, from about 20 Ma the Site U1356 path from about 59°S to a more southern paleolatitude accelerated and the site crossed through the main flow tract of the wind-driven ACC (Scher et al., 2015). Furthermore, an increase in sediment supply to offshore depocenters as ice sheets retreated in combination with a stronger contour current, may have produced the sediment waves that are visible in the seismic data overlying the Upper Oligocene channels-levee systems (Figure 2). Similar Upper Oligocene/Lower Miocene sediment waves produced by the interaction of downslope currents and contour currents are present in a levee drift west of the Prydz Channel on the same passive margin of Antarctica (Kuvaas & Leitchenkov, 1992).

We interpret the facies associations (Figures 9C, 9D) in this interval of core as cyclical alternations of hemipelagic sedimentation with hyperpycnal flows, with the strongest downslope currents indicated by the ripple cross-laminated sandstone interbeds (Figure 9C). The structure of the graded sand bed at 329 mbsf (Figure 3) is interpreted as a distal turbidite indicative of overbank deposition from active nearby deep-sea channels (Mulder *et al.* 2003; Lamb & Mohrig 2009; Mutti *et al.* 2009). The more homogeneous hemipelagic units likely signal times with stronger interaction between contour currents and downslope flow that could have impacted flow rheology (Cantero *et al.* 2011). Ice rafting over the drillsite was probably limited during the early Miocene given the paucity of outsized clasts between 442 and 278 mbsf (Figure 3).

Site U1356 Unit G: Middle Miocene (0-278 mbsf) – hemipelagic sedimentation

The upper 278 meters below seafloor in Hole U1356A (Cores 1R-28R) are dominated by diatom ooze and diatomaceous clayey silt with dispersed gravel (Figure 3). Below 126 mbsf, where the formation is more indurated and, therefore, better preserved in rotary drilling, clast-poor diatom-rich beds locally preserve an interlaminated structure of clay-rich diatom ooze and diatom-rich silty clay (Figure 9A). Clast-rich mudstones are interbedded with laminated silty claystones and display vertical flow structures and clast nests (Figure 9B). Disorganized clast-rich mudstones and diamictites with intraclasts are also present at the base of this interval (Expedition 318 Scientists 2011a).

The particle size distributions of the samples in Unit G show a lot of variability in sand-silt-clay content (Figure 4). Some sand-rich sediments are poorly sorted (uniformity 4 or higher), however, the sediments with the highest sand percentage (>50%) show a relatively low uniformity and grains with a slightly higher shape index of ~0.3 (more spherical), indicative of episodic current sorting and winnowing. These latter sediments occur in an interval with an absence of gravel in the sediment.

We interpret the facies assemblage in this Unit as hemipelagic deposition in an ice-influenced environment with episodic turbidity current activity. In deep-water settings, laminated diatom oozes (Figure 9A) are typically found beneath ocean fronts, such as the Polar Front in the Southern Ocean (Zielinski & Gersonde, 1997; Kemp *et al.* 2006). Analyses of the specific diatom species is necessary, however, to reconstruct the exact particle transport paths for these sedimentary units. The vertical soft-sediment flow structures and clast clusters (Figure 9B) are typical of IRD (Bennett *et al.* 1996; Licht et al, 1998; Kilfeather *et al.* 2010). The disorganized clast-rich mudstones and diamictites with intraclasts represent gravity flow facies.

The mid-Miocene depositional environments of Site U1356 are characterized by intermittent cold periods with seasonal sea ice and fast ice trapping icebergs nearshore, and hemipelagic sedimentation similar to today interrupted by episodes of extensive ice rafting. Two clast rich intervals indicating ice rafting occur between ca.14.5 and 13.5 Ma. The presence of extensive IRD in some portions of the mid-Miocene interval at Site U1356A requires a different ocean circulation pattern to that of the present day interglacial, possibly including an episodic weakening of the westward-flowing Polar Current, or the presence of large ice sheets at the continental shelf break that were vulnerable to collapse due to contact with warm ocean currents.

Controls on changes in sedimentation

The sedimentary facies in most modern deepwater depositional systems are best studied on low latitude passive margins (e.g., the Amazon Fan), whereas ancient examples of sedimentary facies associations have primarily been described from convergent margins, e.g. European Alpine systems, New Zealand, and Appalachian basin. Our study is unique in that it addresses deposition using sedimentological data collected at a high latitude passive margin, which has some fundamental differences with the settings mentioned above.

One of the main differences is the effect of ice growth on the creation of shelf depocenters and off-shore sediment transport (Boulton 1990; Powell & Cooper 2002; Passchier *et al.* 2013; Stocchi *et al.* 2013). Middle Eocene shallow marine strata at Site U1356 show a shoaling and are terminated by an unconformity, which is consistent with the development of a forebulge offshore and a reduction in accommodation. The lowermost Oligocene strata show a glacial influence with some gravity flows consistent with major early Oligocene glaciation (Houben *et al.* 2013). Overlying these strata, however, is a thick succession with very limited evidence of downslope gravity flow. Stocchi *et al.* (2013) showed in a geodynamic model how the major Oligocene glaciation created a moat of several hundreds of meters deep around on the Antarctic continental shelf. We envision an early Oligocene ice sheet on the continental shelf that trapped glaciogenic sediments in these newly developed depocenters. The remarkably uniform lower Oligocene glacigenic facies recovered in the lower section of Hole U1360 lend strong support to this model.

With our new data we build upon the depositional models of Boulton (1990) for glacial continental margins and those of Pudsey (2000), Lucchi *et al.* (2002) and Hepp *et al.* (2006) for Antarctic Peninsula drift deposits. Both the Wilkes Land/George V Land and the Antarctic Peninsula margin have a narrow continental shelf and the facies cyclicity of bottom current deposits shows similarities. The facies cyclicity observed at Site U1356 is most likely also related to glacial-interglacial changes in sediment delivery to the continental rise by gravity flows (Figure 10). We deviate slightly from previous facies models, however, in that we apply relative sea level changes that envision a sea level rise during glacial times and a relative sea level fall during interglacial times. This assumption takes care of the need for unrealistic abrupt interglacial to glacial transitions that are problematic in previous depositional models (see Hepp *et al.* 2006, p.192). Previously the transitions between glacial and interglacial phases were assumed to coincide exactly with lithological boundaries. However, such a tight coupling is unlikely considering the delayed response of glacio-isostatic processes during glacial-interglacial transitions, and the resulting latitudinal shifts in the loci of erosion and deposition (Boulton, 1990).

Before the termination of each glacial period, the marine ice sheets were likely affected by upwelling of relatively warm circumpolar deepwater, which intensified as the ocean frontal systems moved southward toward the glaciated margin. In our model, the gradational basal contacts of the bioturbated subfacies reflect the gradual onsets of glacial phases and the relatively slow process of ice advance (Figure 10, early glacial stage). The top of the bioturbated subfacies typically contains ice-rafted debris and nannofossil or biosilica-rich beds, signaling intensified ice-rafting and enhanced productivity as marine-based ice-sheets retreated from the outer continental shelf. Enhanced ice-rafting and nannofossil productivity at East Antarctic continental rise sites also accompanied the onset of the retreat of the Antarctic ice sheet in more recent times (Villa *et al.* 2008; Weber *et al.* 2014).

Sharp-based clay-rich laminated facies with silt ripples or sandy debrites, represent the abrupt onset of sediment-laden hyperpycnal flows. On glaciated continental margins hyperpycnal flows can be generated through three processes that enhance sediment load, salinity, and temperature respectively: 1) as rivers discharge into the ocean during floods, which are typically augmented in lateglacial times (Mulder *et al.* 2003; Hesse & Khodabakhsh 2006; Jorry *et al.* 2011); 2) as hyper saline density flows export high-salinity shelf water originating from sea-ice brines (Harris *et al.* 2001); 3) as supercooled ice-shelfwater discharges from the grounding line of an ice sheet on the continental shelf (Dieckmann *et al.* 1986). Sediment-poor density flows that are generated from hyper salinity or supercooling cannot be expected to generate thick units of laminated fine-grained hemipelagic sediment. More likely, the sharp-based clay-rich laminated facies with silt ripples or sandy debrites,represent the onset of sediment-laden hyperpycnal flows from sediment bypassing of the shelf as relative sea level dropped due to post-glacial steric processes and isostatic rebound (Figure 10, lateglacial stage). Furthermore, due to the strong Coriolis Effect at higher latitude hyperpycnal flows were strongly deflected westward in the Southern Hemisphere and sediment focusing in depocenters was controlled by the interplay of hyperpycnal flows and contour currents (Rebesco *et al.* 1996). As deglaciation progressed, the sedimentation became more pelagic with an increase in bioturbation during interglacial stages and into the next early glacial stage (Figure 10).

CONCLUDING REMARKS

The strong potential impact of GIA processes on accommodation affects the sequence stratigraphic interpretations of high-latitude continental margins. Changes in Cenozoic Antarctic ice volume are relatively well-constrained from deep-sea benthic isotope records (Zachos *et al.* 2001; 2008). During times of large ice volumes, such as the early Oligocene and mid-Miocene, cyclic sedimentation of hemipelagic facies and muddy turbidites/contourites prevailed, with the coarse grained sediment accumulating on the continental shelf. It is possible that the low concentrations of IRD were due to a strong coast-parallel Polar Current, keeping IRD in circulation near the Antarctic continental margin. In contrast, during times of smaller ice volume, such as the late Oligocene, sandy debris flows occurred on the Antarctic margin. The early Oligocene was a time of large sediment supply and channel levee building off Wilkes Land, and decreasing accommodation on the passive margin shelf. These results suggest that sequence stratigraphic models designed for low-latitude passive margins do not work in interpretations of high-latitude stratigraphy.

The key element is, that in icehouse phases relative sea level changes are opposite on low and high latitude margins with nearby ice growth due to the effects of GIA (Boulton, 1990; Stocchi *et al.* 2013). On high latitude continental margins, relative sea level is high during glacial phases, and low during interglacial phases. As a consequence, fine-grained bioturbated deposits represent the onsets of ice growth phases, whereas sandy gravity flow deposits represent the onsets of the ice sheet minima.

Acknowledgements

This research used samples provided by the International Ocean Discovery Program. Shipboard participation by S. Passchier on IODP Expedition 318 and post-cruise funding was provided through the U.S. Science Support Program. Additional funding for this research came from the U.S. National Science Foundation (award # ANT-1245283) to S. Passchier.

References:

Anderson, R., Ali, S., Bradtmiller, L., Nielsen, S., Fleisher, M., Anderson, B. & Burckle, L. 2009. Wind-driven upwelling in the Southern Ocean and the deglacial rise in atmospheric CO2. Science, 323, 1443-1448.

Bennett, M.R., Doyle, P. & Mather, A.E. 1996. Dropstones: their origin and significance. Palaeogeography, Palaeoclimatology, Palaeoecology, 121, 331-339.

Bijl, P.K., Bendle, J.A.P., Bohaty, S.M., Pross, J., Schouten, S., Tauxe, L., Stickley, C.E., McKay, R.M., *et al.* 2013. Eocene cooling linked to early flow across the Tasmanian Gateway. Proceedings of the National Academy of Sciences, 110, 9645-9650, http://doi.org/10.1073/pnas.1220872110.

Böning P., Cuypers S., Grunwald M., Schnetger B., & Brumsack H.-J. 2005. Geochemical Characteristics of Chilean upwelling sediments at ~36°S. Marine Geology 220, 1-21

Boulton, G.S. 1990. Sedimentary and sea level changes during glacial cycles and their control on glacimarine facies architecture. In: Dowdeswell, J.A., Scourse, J.D. (ed) Glacimarine Environments: Processes and Sediments. Geological Society of London, Oxford, 53, 15-52.

Cantero, M.I., Cantelli, A., Pirmez, C., Balachandar, S., Mohrig, D., Hickson, T.A., Yeh, T.-h., Naruse, H., *et al.* 2011. Emplacement of massive turbidites linked to extinction of turbulence in turbidity currents. Nature Geoscience, 5, 42-45, http://doi.org/10.1038/ngeo1320.

Cleveringa, J. 2001. Reconstruction and modelling of Holocene coastal evolution of the western Netherlands.

Close, D.I. 2010. Slope and fan deposition in deep-water turbidite systems, East Antarctica. Marine Geology, 274, 21-31, http://doi.org/10.1016/j.margeo.2010.03.002.

Close, D.I., Watts, A.B. & Stagg, H.M.J. 2009. A marine geophysical study of the Wilkes Land rifted continental margin, Antarctica. Geophysical Journal International, 177, 430-450, http://doi.org/10.1111/j.1365-246X.2008.04066.x.

Damuth, J.E. & Fairbridge, R.W. 1970. Equatorial Atlantic deep-sea arkosic sands and ice-age aridity in tropical South America. Geological Society of America Bulletin, 81, 189-206.

De Santis L., Brancolini G., Donda F., 2003. Seismo-stratigraphic analysis of the Wilkes Land continental margin (East Antarctica). Deep Sea Research Special Volume II, 50, 8-9, 1563-1594.

De Santis, L., Brancolini, G., Donda, F. & O'Brien, P. 2010. Cenozoic deformation in the George V Land continental margin (East Antarctica). Marine Geology, 269, 1-17, http://doi.org/10.1016/j.margeo.2009.12.001.

DeConto, R.M. & Pollard, D. 2003. Rapid Cenozoic glaciation of Antarctica induced by declining atmospheric CO2. Nature, 421, 245-249.

Dieckmann, G., Rohardt, G., Hellmer, H. & Kipfstuhl, J. 1986. The occurrence of ice platelets at 250 m depth near the Filchner Ice Shelf and its significance for sea ice biology. Deep Sea Research Part A. Oceanographic Research Papers, 33, 141-148, http://doi.org/http://dx.doi.org/10.1016/0198-0149(86)90114-7.

Donda, F., Brancolini, G., De Santis, L. & Trincardi, F. 2003. Seismic facies and sedimentary processes on the continental rise off Wilkes Land (East Antarctica): evidence of bottom current activity. Deep Sea Research Part II: Topical Studies in Oceanography, 50, 1509-1527.

Donda, F., O'Brien, P.E., De Santis, L., Rebesco, M. & Brancolini, G. 2008. Mass wasting processes in the Western Wilkes Land margin: Possible implications for East Antarctic glacial history. Palaeogeography, Palaeoclimatology, Palaeoecology, 260, 77-91, http://doi.org/10.1016/j.palaeo.2007.08.008.

Dunlea, A.G., Murray, R.W., Sauvage, J., Spivack, A.J., Harris, R.N. & D'Hondt, S. 2015. Dust, volcanic ash, and the evolution of the South Pacific Gyre through the Cenozoic. Paleoceanography, 30, 1078-1099, http://doi.org/10.1002/2015pa002829.

Escutia, C., Brinkhuis, H. & Klaus, A. the Expedition 318 Scientists (2011), Site U1356. Proc. IODP, 318.

Escutia, C., Eittreim, S., Cooper, A. & Nelson, C. 2000. Morphology and acoustic character of the Antarctic Wilkes Land turbidite systems: ice-sheet-sourced versus river-sourced fans. Journal of Sedimentary Research, 70, 84-93.

Escutia, C., Nelson, C., Acton, G., Eittreim, S., Cooper, A., Warnke, D. & Jaramillo, J. 2002. Current controlled deposition on the Wilkes Land continental rise, Antarctica. Geological Society, London, Memoirs, 22, 373-384.

Escutia, C., De Santis, L., Donda, F., Dunbar, R.B., Cooper, A.K., Brancolini, G. & Eittreim, S.L. 2005. Cenozoic ice sheet history from East Antarctic Wilkes Land continental margin sediments. Global and Planetary Change, 45, 51-81, http://doi.org/10.1016/j.gloplacha.2004.09.010.

Expedition 318 Scientists, 2011a. Site U1356. In Escutia, C., Brinkhuis, H., Klaus, A., and the Expedition 318 Scientists, Proc. IODP, 318: Tokyo (Integrated Ocean Drilling Program Management International, Inc.). doi:10.2204/iodp.proc.318.104.2011

Expedition 318 Scientists, 2011b. Site U1360. In Escutia, C., Brinkhuis, H., Klaus, A., and the Expedition 318 Scientists, Proc. IODP, 318: Tokyo (Integrated Ocean Drilling Program Management International, Inc.). doi:10.2204/iodp.proc.318.108.2011

Goldner, A., Herold, N. & Huber, M. 2014. Antarctic glaciation caused ocean circulation changes at the Eocene–Oligocene transition. Nature 511, 574–577, http://doi.org/10.1038/nature13597

Hansen, M.A. 2011. Determining Middle Miocene through Pliocene changes in provenance and basal ice conditions through sedimentological analyses of subglacial diamictites in AND-2A, Ross Sea, Antarctica. M.S. Thesis, Montclair State University, 116p.

Harris, P.T., Brancolini, G., Armand, L., Busetti, M., Beaman, R.J., Giorgetti, G., Presti, M. & Trincardi, F. 2001. Continental shelf drift deposit indicates non-steady state Antarctic bottom water production in the Holocene. Marine Geology, 179, 1-8.

Haughton, P., Davis, C., McCaffrey, W. & Barker, S. 2009. Hybrid sediment gravity flow deposits – Classification, origin and significance. Marine and Petroleum Geology, 26, 1900-1918, http://doi.org/10.1016/j.marpetgeo.2009.02.012.

Hepp, D.A., Mörz, T. & Grützner, J. 2006. Pliocene glacial cyclicity in a deep-sea sediment drift (Antarctic Peninsula Pacific Margin). Palaeogeography, Palaeoclimatology, Palaeoecology, 231, 181-198, http://doi.org/10.1016/j.palaeo.2005.07.030.

Hodgson, D.M. 2009. Distribution and origin of hybrid beds in sand-rich submarine fans of the Tanqua depocentre, Karoo Basin, South Africa. Marine and Petroleum Geology, 26, 1940-1956, http://doi.org/10.1016/j.marpetgeo.2009.02.011.

Houben, A.J., Bijl, P.K., Pross, J., Bohaty, S.M., Passchier, S., Stickley, C.E., Rohl, U., Sugisaki, S., *et al.* 2013. Reorganization of Southern Ocean plankton ecosystem at the onset of Antarctic glaciation. Science, 340, 341-344, http://doi.org/10.1126/science.1223646.

Kemp, A.E.S., Pearce, R.B., Grigorov, I., Rance, J., Lange, C.B., Quilty, P. & Salter, I. 2006. Production of giant marine diatoms and their export at oceanic frontal zones: Implications for Si and C flux from stratified oceans. Global Biogeochemical Cycles, 20, n/a-n/a, http://doi.org/10.1029/2006gb002698.

Kilfeather, A.A., Cofaigh, C.Ó., Dowdeswell, J.A., van der Meer, J.J. & Evans, D.J. 2010. Micromorphological characteristics of glacimarine sediments: implications for distinguishing genetic processes of massive diamicts. Geo-Marine Letters, 30, 77-97.

Konert, M. & Vandenberghe, J. 1997. Comparison of laser grain size analysis with pipette and sieve analysis: a solution for the underestimation of the clay fraction. Sedimentology, 44, 523-535.

Kvenvolden, K.A. 1993. Gas hydrates—geological perspective and global change. Reviews of Geophysics, 31, 173-187, http://doi.org/10.1029/93RG00268.

Lamb, M.P. & Mohrig, D. 2009. Do hyperpycnal-flow deposits record river-flood dynamics? Geology, 37, 1067-1070, http://doi.org/10.1130/g30286a.1.

Lucchi, R., Rebesco, M., Camerlenghi, A., Busetti, M., Tomadin, L., Villa, G., Persico, D., Morigi, C., *et al.* 2002. Mid-late Pleistocene glacimarine sedimentary processes of a high-latitude, deep-sea sediment drift (Antarctic Peninsula Pacific margin). Marine Geology, 189, 343-370.

Martin, L. & Passchier, S. 2010. Basal Ice Conditions of the Antarctic Ice Sheet interpreted from Oligocene through Pleistocene tills of the Cape Robert Drilling Project. Geological Society of America Abstracts with Programs, v. 42 n.1 p.170.

Maslin, M., Mikkelsen, N., Vilela, C. & Haq, B. 1998. Sea-level–and gas-hydrate–controlled catastrophic sediment failures of the Amazon Fan. Geology, 26, 1107-1110.

Mazzullo, J., Graham, A.G. & Braunstein, C. 1988. Handbook for shipboard sedimentologists. Ocean Drilling Program.

McCave, I. 2008. Size sorting during transport and deposition of fine sediments: sortable silt and flow speed. Developments in Sedimentology, 60, 121-142.

McHugh, C.M., Hartin, C.A., Mountain, G.S. & Gould, H.M. 2010. The role of glacio-eustasy in sequence formation: Mid-Atlantic Continental Margin, USA. Marine Geology, 277, 31-47, http://doi.org/10.1016/j.margeo.2010.08.009.

Miller, S.R., Fitzgerald, P.G. & Baldwin, S.L. 2010. Cenozoic range-front faulting and development of the Transantarctic Mountains near Cape Surprise, Antarctica: Thermochronologic and geomorphologic constraints. Tectonics, 29, n/a-n/a, http://doi.org/10.1029/2009tc002457.

Miller, K.G., Sugarman, P.J., Browning, J.V., Kominz, M.A., Olsson, R.K., Feigenson, M.D. & Hernández, J.C. 2004. Upper Cretaceous sequences and sea-level history, New Jersey coastal plain. Geological Society of America Bulletin, 116, 368-393.

Moncrieff, A. 1989. Classification of poorly-sorted sedimentary rocks. Sedimentary Geology, 65, 191-194.

Mulder, T., Syvitski, J.P.M., Migeon, S., Faugères, J.-C. & Savoye, B. 2003. Marine hyperpycnal flows: initiation, behavior and related deposits. A review. Marine and Petroleum Geology, 20, 861-882, http://doi.org/10.1016/j.marpetgeo.2003.01.003.

Murray, R., Miller, D.J. & Kryc, K. 2000. Analysis of major and trace elements in rocks, sediments, and interstitial waters by inductively coupled plasma–atomic emission spectrometry (ICP-AES).

Mutti, E., Bernoulli, D., Lucchi, F.R. & Tinterri, R. 2009. Turbidites and turbidity currents from Alpine 'flysch' to the exploration of continental margins. Sedimentology, 56, 267-318, http://doi.org/10.1111/j.1365-3091.2008.01019.x.

Owens, J. & Sohl, N. 1969. Shelf and deltaic paleoenvironments in the Cretaceous-Tertiary formations of the New Jersey Coastal Plain. Geology of Selected Areas in New Jersey and Eastern Pennsylvania and Guidebook of Excursions: New Brunswick, NJ (Rutgers Univ. Press).

Passchier, S. & Kleinhans, M.G. 2005. Observations of sand waves, megaripples, and hummocks in the Dutch coastal area and their relation to currents and combined flow conditions. Journal of Geophysical Research, 110, http://doi.org/10.1029/2004jf000215.

Passchier, S., Falk., C. & Florindo, F., 2013. Orbitally-paced shifts in the particle size of the Antarctic continental shelf in response to ice dynamics during the Miocene Climatic Optimum. Geosphere, 9, 54-62, http://doi.org/10.1130/GES00840.1.

Passchier, S., Ciarletta, D.J., Miriagos, T.E., Bijl, P.K. & Bohaty, S.M. 2017. An Antarctic stratigraphic record of stepwise ice growth through the Eocene-Oligocene transition. Geological Society of America Bulletin, 129, 3/4, 318–330, http://doi.org/10.1130/B31482.1.

Passchier, S., Bohaty, S.M., Jiménez-Espejo, F., Pross, J., Röhl, U., van de Flierdt, T., Escutia, C. & Brinkhuis, H. 2013. Early Eocene to middle Miocene cooling and aridification of East

Antarctica. Geochemistry, Geophysics, Geosystems, 14, 1399-1410, http://doi.org/10.1002/ggge.20106.

Paull, C.K., Buelow, W.J., Ussler, W. & Borowski, W.S. 1996. Increased continental-margin slumping frequency during sea-level lowstands above gas hydrate–bearing sediments. Geology, 24, 143-146.

Paytan, A. & Griffith, E.M. 2007. Marine barite: Recorder of variations in ocean export productivity. Deep Sea Research Part II: Topical Studies in Oceanography, 54, 687-705.

Peakall, J., Kane, I.A., Masson, D.G., Keevil, G., McCaffrey, W. & Corney, R. 2012. Global (latitudinal) variation in submarine channel sinuosity. Geology, 40, 1, 11–14. https://doi.org/10.1130/G32295.1

Pondaven, P., Ragueneau, O., Tréguer, P., Hauvespre, A., Dezileau, L. & Reyss, J.L. 2000. Resolving the ‘opal paradox’in the Southern Ocean. Nature, 405, 168-172.

Powell, R.D. & Cooper, J.M. 2002. A glacial sequence stratigraphic model for temperate, glaciated continental shelves. Geological Society, London, Special Publications, 203, 215-244, https://doi.org/10.1144/GSL.SP.2002.203.01.12

Pross, J., Contreras, L., Bijl, P.K., Greenwood, D.R., Bohaty, S.M., Schouten, S., Bendle, J.A., Rohl, U., *et al*. 2012. Persistent near-tropical warmth on the Antarctic continent during the early Eocene epoch. Nature, 488, 73-77, http://doi.org/10.1038/nature11300.

Pudsey, C. 2000. Sedimentation on the continental rise west of the Antarctic Peninsula over the last three glacial cycles. Marine Geology, 167, 313-338.

Rebesco, M., Larter, R.D., Camerlenghi, A. & Barker, P.F. 1996. Giant sediment drifts on the continental rise west of the Antarctic Peninsula. Geo-Marine Letters, 16, 65-75.

Röhl, U., Brinkhuis, H., Sluijs, A. & Fuller, M. 2004. On the search for the Paleocene/Eocene boundary in the Southern Ocean: exploring ODP Leg 189 Holes 1171D and 1172D, Tasman Sea. The Cenozoic Southern Ocean: Tectonics, Sedimentation, and Climate Change Between Australia and Antarctica, 113-125.

Rijsdijk, K.F., Passchier, S., Weerts, H.J.T, Laban, C., Van Leeuwen, R.J. & Ebbing, J.H., 2005. Revised Upper Cenozoic stratigraphy of the Dutch sector of the North Sea basin: towards an integrated lithostratigraphic, seismostratigraphic, and allostratigraphic approach. Netherlands Journal of Geosciences, 84, 2, 129-146.

Schenau, S., Prins, M.A., De Lange, G.J. & Monnin, C., 2001. Barium accumulation in the Arabian Sea: Controls on barite preservation in marine sediments. Geochimica et Cosmochimica Acta 65, 10, 1545-1556, http://doi.org/10.1016/S0016-7037(01)00547-6.

Scher, H.D., Whittaker, J.M., Williams, S.E., Latimer, J.C., Kordesch, W.E. & Delaney, M.L. 2015. Onset of Antarctic Circumpolar Current 30 million years ago as Tasmanian Gateway aligned with westerlies. Nature, 523, 580-583, http://doi.org/10.1038/nature14598.

Shanmugam, G. 2006. The Tsunamite Problem. Journal of Sedimentary Research, 76, 718-730, http://doi.org/10.2110/jsr.2006.073.

Sperazza, M., Moore, J.N. & Hendrix, M.S. 2004. High-resolution particle size analysis of naturally occurring very fine-grained sediment through laser diffractometry. Journal of Sedimentary Research, 74, 736-743.

Stanley, D.J., 1988. Turbidites reworked by bottom currents : upper Cretaceous examples from St. Croix, U.S. Virgin Islands. Smithsonian contributions to the marine sciences, 33, 79p.

Stocchi, P., Escutia, C., Houben, A.J.P., Vermeersen, B.L.A., Bijl, P.K., Brinkhuis, H., DeConto, R.M., Galeotti, S., *et al.* 2013. Relative sea-level rise around East Antarctica during Oligocene glaciation. Nature Geoscience, 6, 380-384, http://doi.org/10.1038/ngeo1783.

Stuart, K.M. & Long, D.G. 2011. Tracking large tabular icebergs using the SeaWinds Ku-band microwave scatterometer. Deep Sea Research Part II: Topical Studies in Oceanography, 58, 1285-1300, http://doi.org/http://dx.doi.org/10.1016/j.dsr2.2010.11.004.

Tauxe, L., Stickley, C.E., Sugisaki, S., Bijl, P.K., Bohaty, S.M., Brinkhuis, H., Escutia, C., Flores, J.A., *et al.* 2012. Chronostratigraphic framework for the IODP Expedition 318 cores from the Wilkes Land Margin: Constraints for paleoceanographic reconstruction. Paleoceanography, 27, http://doi.org/10.1029/2012pa002308.

Toggweiler, J.R., Russell, J.L. & Carson, S.R. 2006. Midlatitude westerlies, atmospheric CO2, and climate change during the ice ages. Paleoceanography, 21.

Uenzelmann-Neben, G. & Gohl, K., 2014. Early glaciation already during the Early Miocene in the Amundsen Sea, Southern Pacific: Indications from the distribution of sedimentary sequences, Global and Planetary Change, 120 , 92-104, http://doi.org/10.1016/j.gloplacha.2014.06.004

van Hinsbergen, D.J., de Groot, L.V., van Schaik, S.J., Spakman, W., Bijl, P.K., Sluijs, A., Langereis, C.G. & Brinkhuis, H. 2015. A paleolatitude calculator for paleoclimate studies. PLoS One, 10, e0126946.

Villa, G., Lupi, C., Cobianchi, M., Florindo, F. & Pekar, S.F. 2008. A Pleistocene warming event at 1 Ma in Prydz Bay, East Antarctica: Evidence from ODP Site 1165. Palaeogeography, Palaeoclimatology, Palaeoecology, 260, 230-244, http://doi.org/10.1016/j.palaeo.2007.08.017.

Weber, M.E., Clark, P.U., Kuhn, G., Timmermann, A., Sprenk, D., Gladstone, R., Zhang, X., Lohmann, G., *et al.* 2014. Millennial-scale variability in Antarctic ice-sheet discharge during the last deglaciation. Nature, 510, 134-138, http://doi.org/10.1038/nature13397.

Wells, M. & Cossu, R. 2013. The possible role of Coriolis forces in structuring large-scale sinuous patterns of submarine channel–levee systems. Phil. Trans. R. Soc. A 371, http://doi.org/10.1098/rsta.2012.0366

Wentworth, C.K. 1922. A scale of grade and class terms for clastic sediments. The Journal of Geology, 30, 377-392.

Wilson, D.S., Jamieson, S.S.R., Barrett, P.J., Leitchenkov, G., Gohl, K. & Larter, R.D. 2012. Antarctic topography at the Eocene–Oligocene boundary. Palaeogeography, Palaeoclimatology, Palaeoecology, 335-336, 24-34, http://doi.org/10.1016/j.palaeo.2011.05.028.

Wright, R. & Anderson, J.B. 1982. The importance of sediment gravity flow to sediment transport and sorting in a glacial marine environment: Eastern Weddell Sea, Antarctica. Geological Society of America Bulletin, 93, 951-963.

Zielinski, U. & Gersonde, R. 1997. Diatom distribution in Southern Ocean surface sediments (Atlantic sector): implications for paleoenvironmental reconstructions. Palaeogeography, Palaeoclimatology, Palaeoecology, 129, 213-250.

Figure Captions:

Figure 1. Antarctic topography during the Eocene-Oligocene with location of drillholes on the Antarctic continental margin. Topographic grid from Wilson *et al.* 2012.

Figure 2. Short seismic line segment GA228-29 through the submarine channel and levee system at IODP drillsite U1356. Major reflector WL-U3 marks the unconformity between middle Eocene and lower Oligocene strata. From Escutia *et al.* 2011.

Figure 3. Lithological log of Site U1356 with gravel clast abundance, Ba-excess, and Si-excess values as determined by ICP-OES analysis.

Figure 4. Lithological log of Site U1356 with grain-size parameters as determined by laser particle size analysis of the matrix (< 2mm). The letters A through G correspond to the stratigraphic units designated in the text.

Figure 5. Detailed graphic log for the lower and middle Eocene and the lower Oligocene strata at Site U1356. The Units A through C correspond to the stratigraphic units designated in the text.

Figure 6. Representative sedimentary facies for the lower and middle Eocene and the lower Oligocene strata at Site U1356. Units A through C correspond to the stratigraphic units designated in the text. The core numbers can be found on the log in Figure 5. The boundary between Units B and C is found at 91 cm in Section 95R3.

Figure 7. Lithological log of recovered strata at Site U1360 with sedimentary facies and particle size distributions.

Figure 8. Lower-middle Oligocene sedimentary facies at Site U1356 are presented in panels A through E, showing particle-size results for each facies paired with one representative image. These facies are interbedded and show cyclicity.

Figure 9. Upper Oligocene-Miocene sedimentary facies at Site U1356 are presented in panels A through E, showing particle-size results for each facies paired with one representative image.

Figure 10. Glacigenic deepwater facies cyclicity and interpretation. Facies association A is found when ice sheets are large and the glaciated margin is built by episodic sediment discharge from meltwater floods and redeposition of slope deposits reworked by contour currents (Lower-mid Oligocene and Miocene of Site U1356). Facies association B is found when ice sheets are small (Upper Oligocene of Site U1356) and high channel levees are built, which generate gravity flows as the channels become active during meltwater or fluvial discharge events. In both cases the mass-gravity flow facies are associated with the onset of deglaciation as the ice sheet begins to retreat from its maximum extent. During this time postglacial rebound and the landward migration of contour currents results in increased sediment delivery to the continental rise.

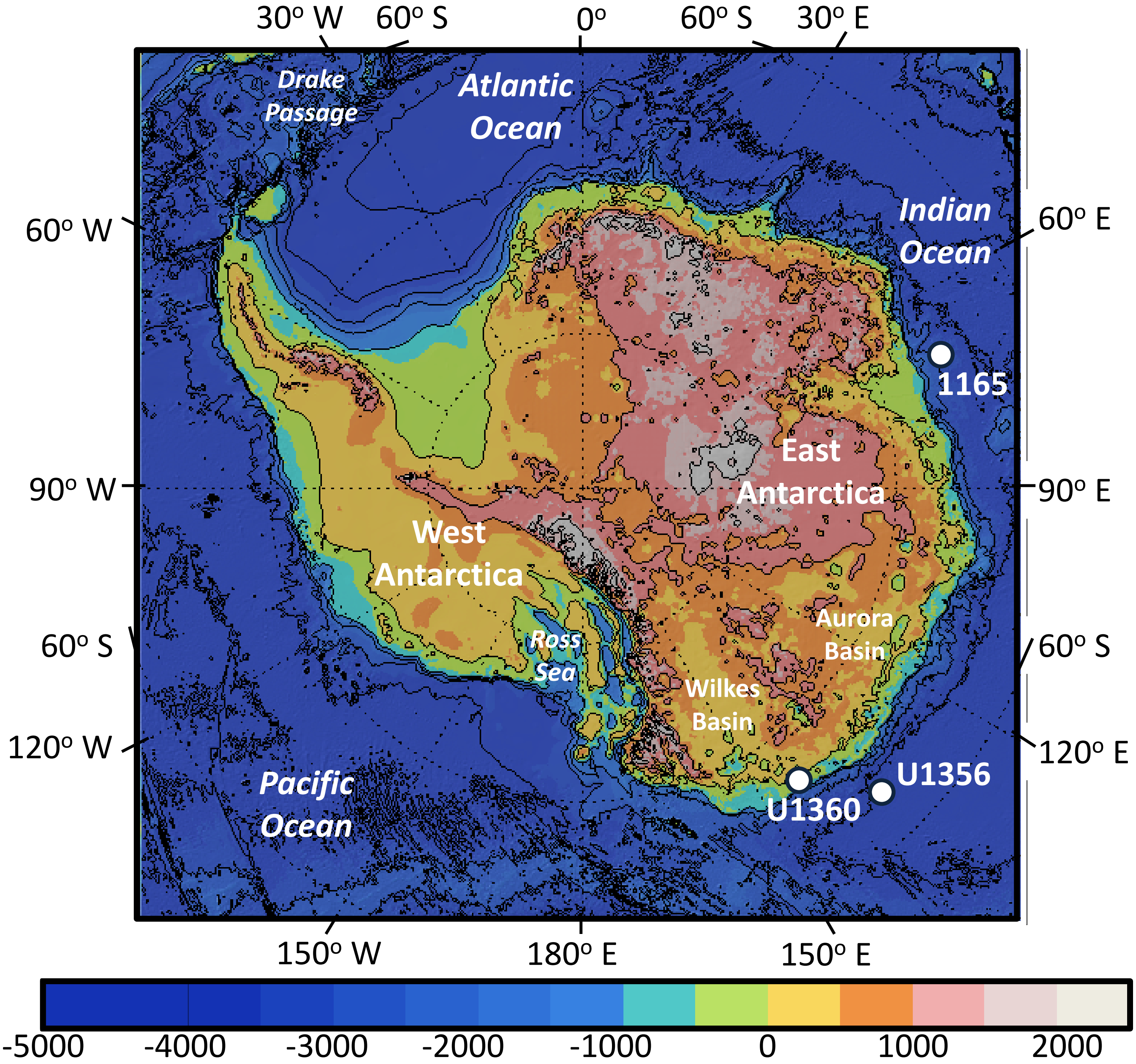
30° W
60° S
0°
60° S
30° E
Drake Passage
Atlantic Ocean
Indian Ocean
60° W
60° E
1165
East Antarctica
90° W
90° E
West Antarctica
Aurora Basin
Ross Sea
60° S
60° S
Wilkes Basin
120° W
120° E
U1356
U1360
Pacific Ocean
150° W
180° E
150° E
-5000
-4000
-3000
-2000
-1000
0
1000
2000

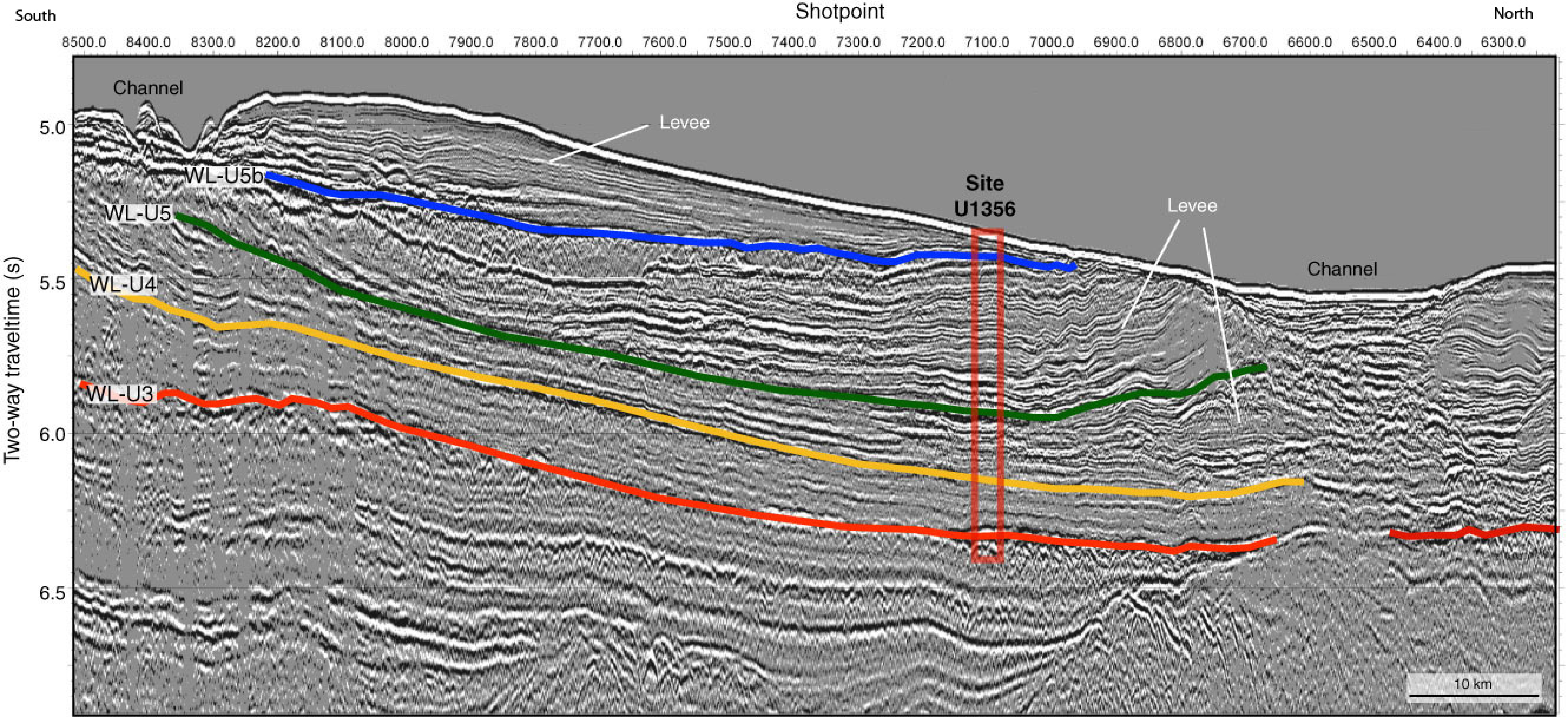
South
Shotpoint
North
8500.0
8400.0
8300.0
8200.0
8100.0
8000.0
7900.0
7800.0
7700.0
7600.0
7500.0
7400.0
7300.0
7200.0
7100.0
7000.0
6900.0
6800.0
6700.0
6600.0
6500.0
6400.0
6300.0
Two-way traveltime (s)
5.0
5.5
6.0
6.5
Channel
Levee
WL-U5b
WL-U5
WL-U4
WL-U3
Site
U1356
Levee
Channel
10 km

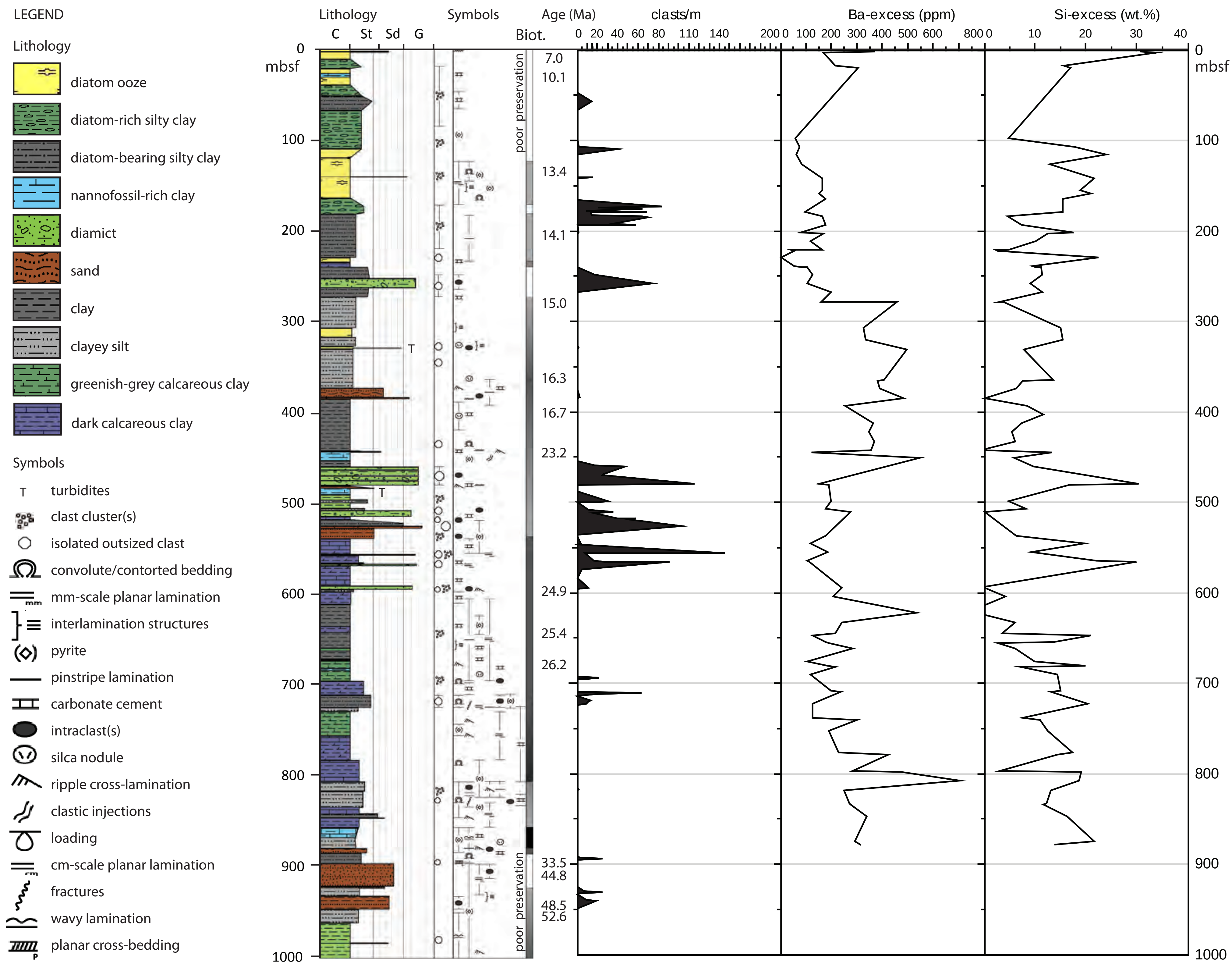

LEGEND
Lithology
diatom ooze
diatom-rich silty clay
diatom-bearing silty clay
nannofossil-rich clay
diamict
sand
clay
clayey silt
greenish-grey calcareous clay
dark calcareous clay
Symbols
turbidites
clast cluster(s)
isolated outsized clast
convolute/contorted bedding
mm-scale planar lamination
interlamination structures
pyrite
pinstripe lamination
carbonate cement
intraclast(s)
silca nodule
ripple cross-lamination
clastic injections
loading
cm-scale planar lamination
fractures
wavy lamination
planar cross-bedding
Lithology
C St Sd G
Symbols
Age (Ma)
Biot.
poor preservation
clasts/m
Ba-excess (ppm)
Si-excess (wt.%)
mbsf
0 100 200 300 400 500 600 700 800 900 1000
7.0 10.1 13.4 14.1 15.0 16.3 16.7 23.2 24.9 25.4 26.2 33.5 44.8 48.5 52.6
0 20 40 60 80 110 140 200
0 100 200 300 400 500 600 800
0 10 20 30 40
T

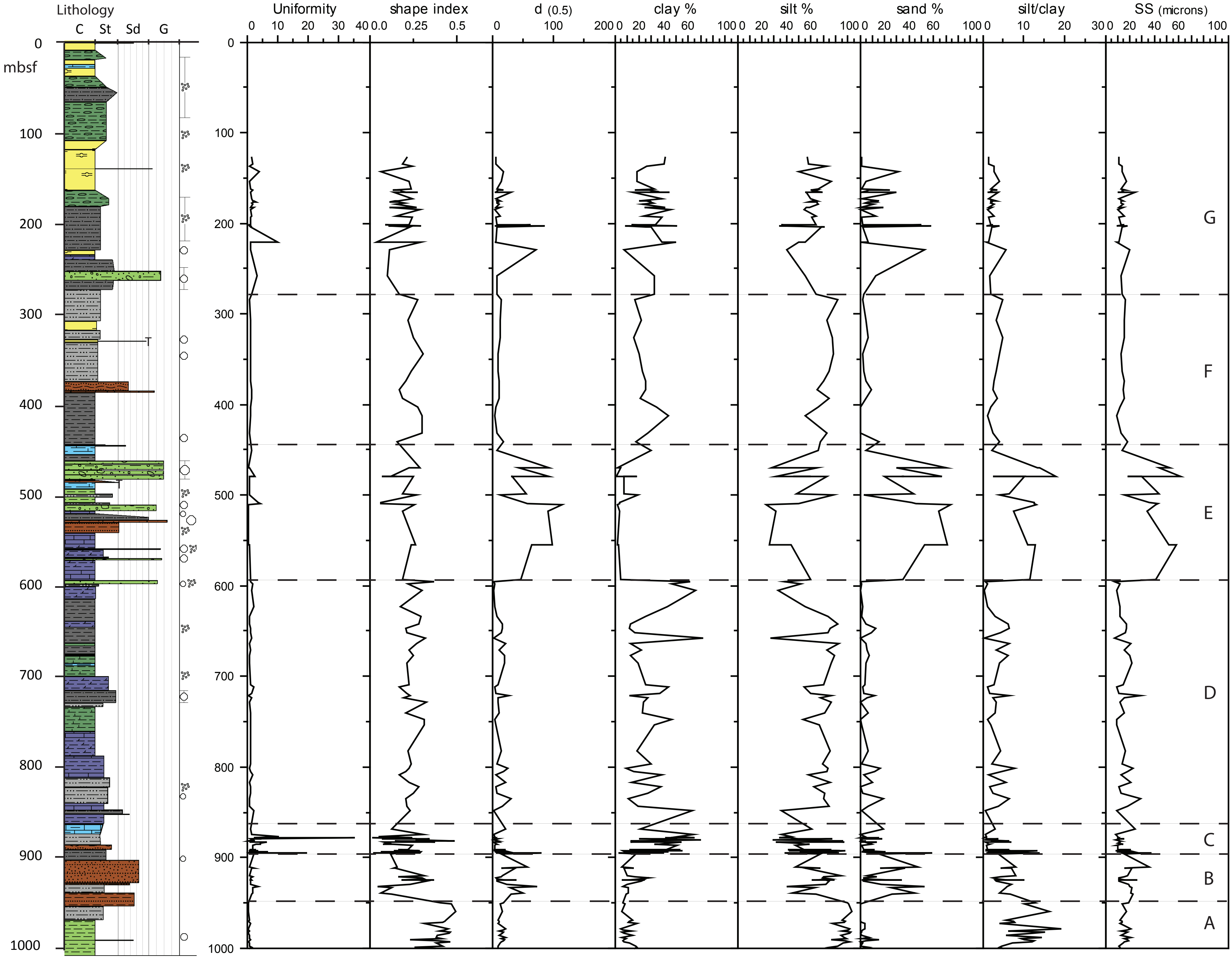

Lithology
C St Sd G
mbsf
Uniformity
shape index
d (0.5)
clay %
silt %
sand %
silt/clay
SS (microns)
0
100
200
300
400
500
600
700
800
900
1000
G
F
E
D
C
B
A

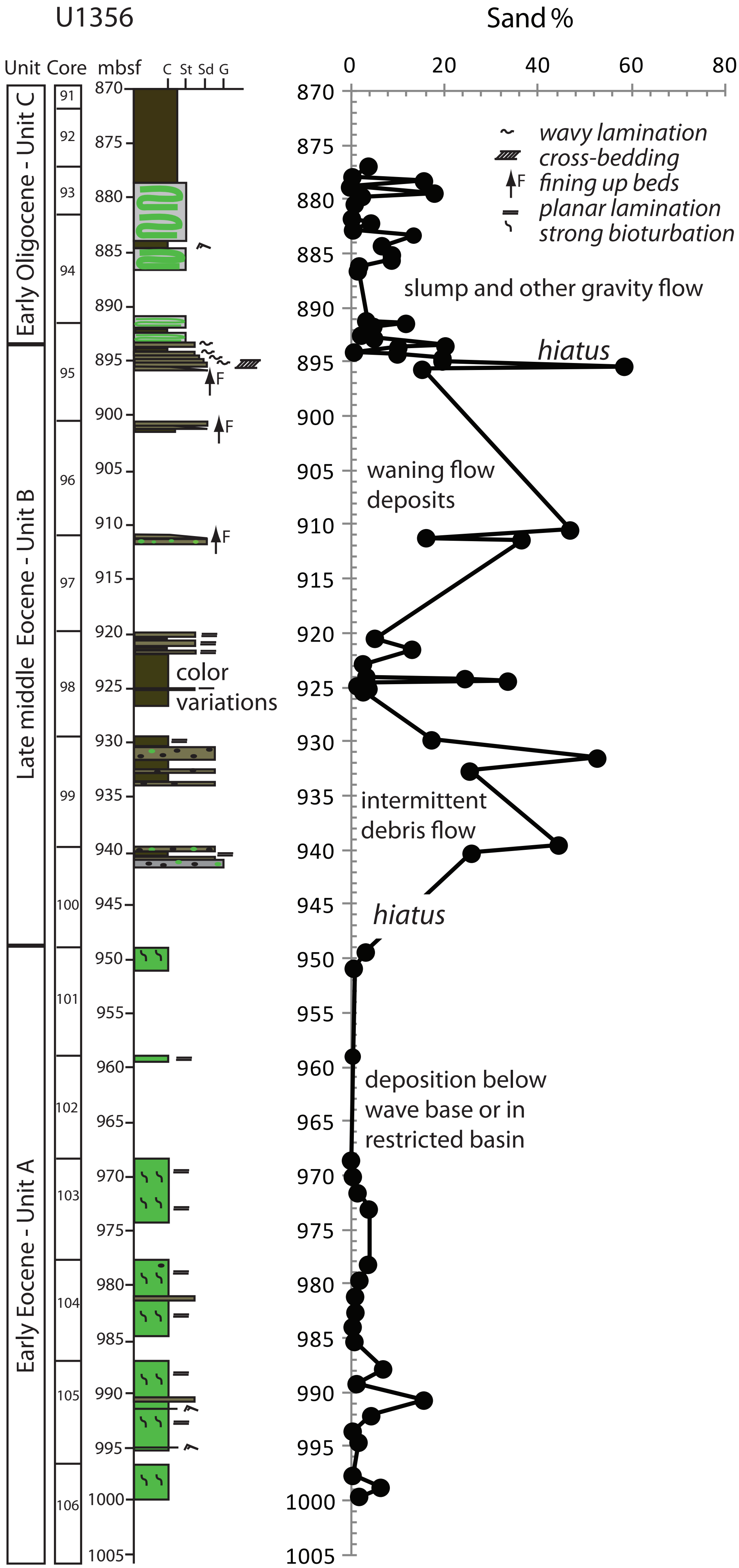

U1356
Sand %
Unit
Core
mbsf
C St Sd G
Early Oligocene - Unit C
Late middle Eocene - Unit B
Early Eocene - Unit A
wavy lamination
cross-bedding
fining up beds
planar lamination
strong bioturbation
slump and other gravity flow
hiatus
waning flow deposits
color variations
intermittent debris flow
hiatus
deposition below wave base or in restricted basin

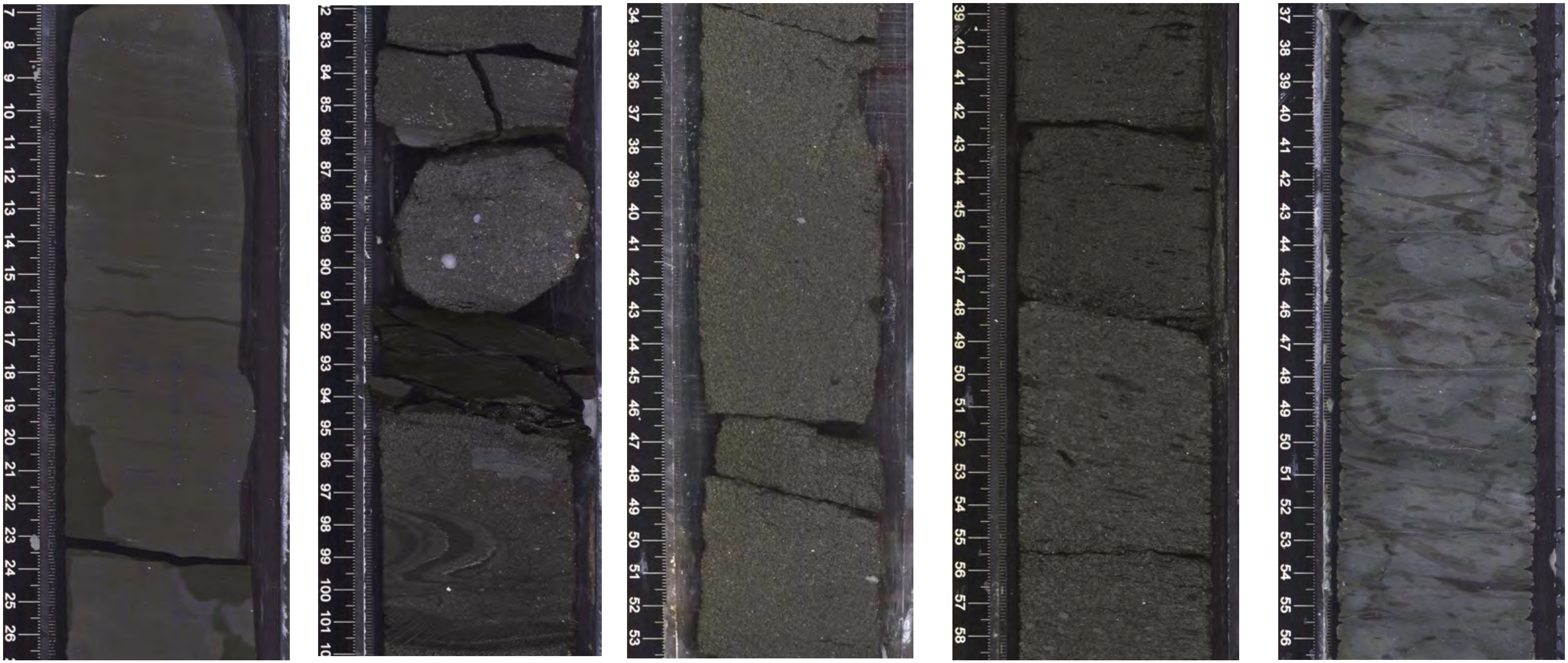
Unit C
Unit C/Unit B
Unit B
Unit B
Unit A
91R1
95R3
95R4
97R1
103R2

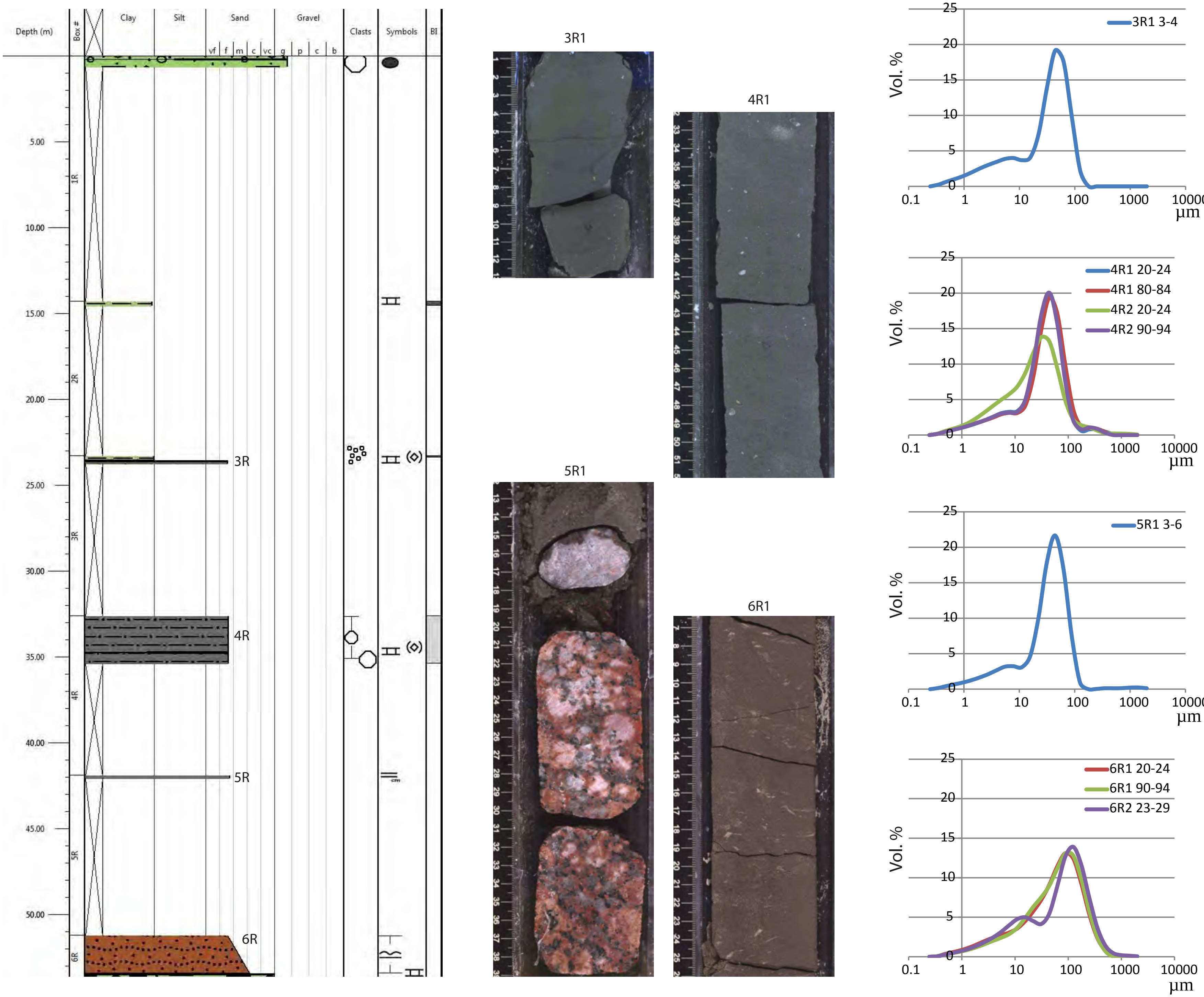

Depth (m)
Box #
Clay
Silt
Sand
Gravel
vf f m c vc g p c b
Clasts
Symbols
BI
5.00
10.00
15.00
20.00
25.00
30.00
35.00
40.00
45.00
50.00
1R
2R
3R
4R
5R
6R
3R
4R
5R
6R
3R1
4R1
5R1
6R1
Vol. %
µm
0.1
1
10
100
1000
10000
3R1 3-4
4R1 20-24
4R1 80-84
4R2 20-24
4R2 90-94
5R1 3-6
6R1 20-24
6R1 90-94
6R2 23-29

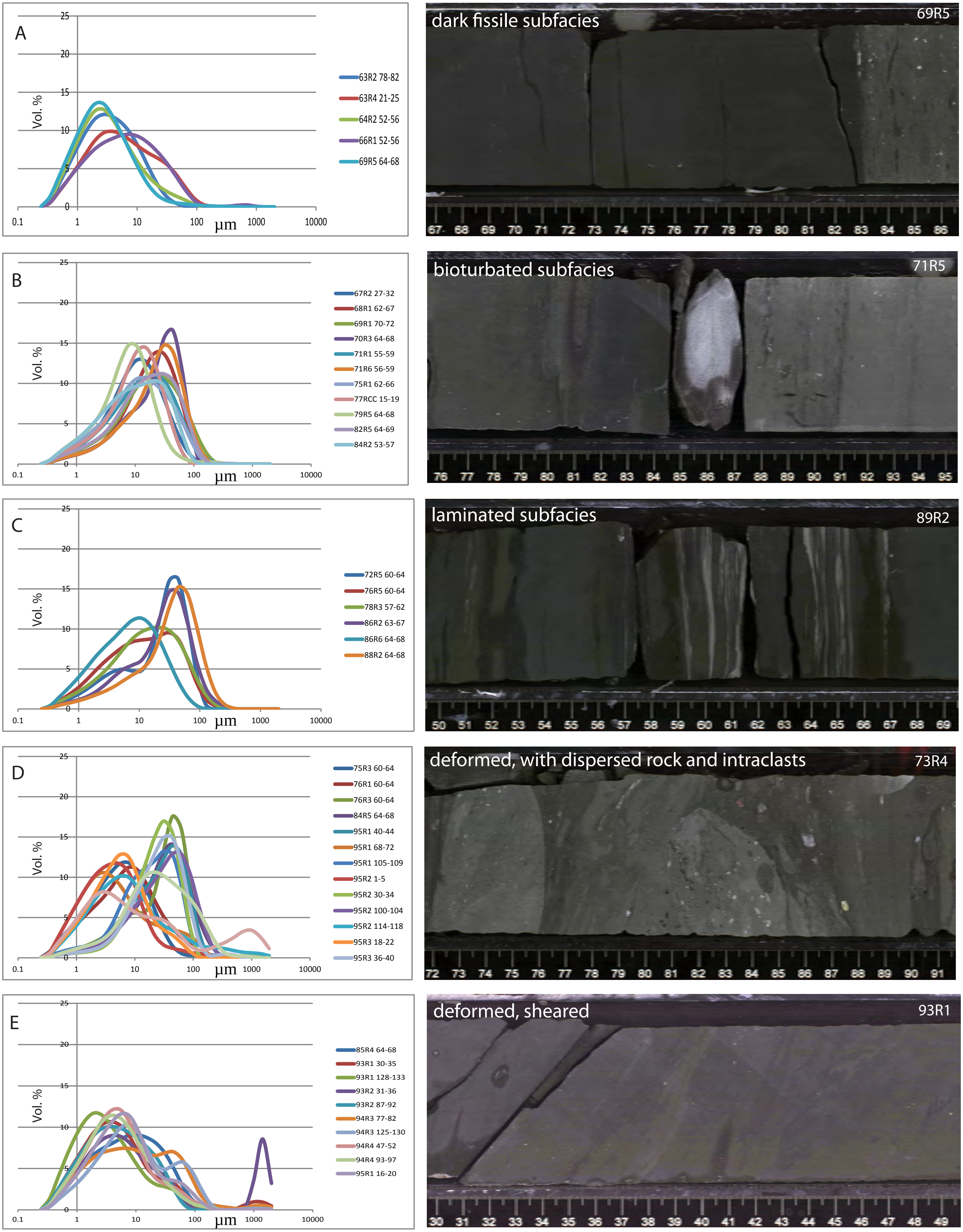
A
Vol. %
µm
0.1
1
10
100
1000
10000
0
5
10
15
20
25
63R2 78-82
63R4 21-25
64R2 52-56
66R1 52-56
69R5 64-68
dark fissile subfacies
69R5
B
67R2 27-32
68R1 62-67
69R1 70-72
70R3 64-68
71R1 55-59
71R6 56-59
75R1 62-66
77RCC 15-19
79R5 64-68
82R5 64-69
84R2 53-57
bioturbated subfacies
71R5
C
72R5 60-64
76R5 60-64
78R3 57-62
86R2 63-67
86R6 64-68
88R2 64-68
laminated subfacies
89R2
D
75R3 60-64
76R1 60-64
76R3 60-64
84R5 64-68
95R1 40-44
95R1 68-72
95R1 105-109
95R2 1-5
95R2 30-34
95R2 100-104
95R2 114-118
95R3 18-22
95R3 36-40
deformed, with dispersed rock and intraclasts
73R4
E
85R4 64-68
93R1 30-35
93R1 128-133
93R2 31-36
93R2 87-92
94R3 77-82
94R3 125-130
94R4 47-52
94R4 93-97
95R1 16-20
deformed, sheared
93R1

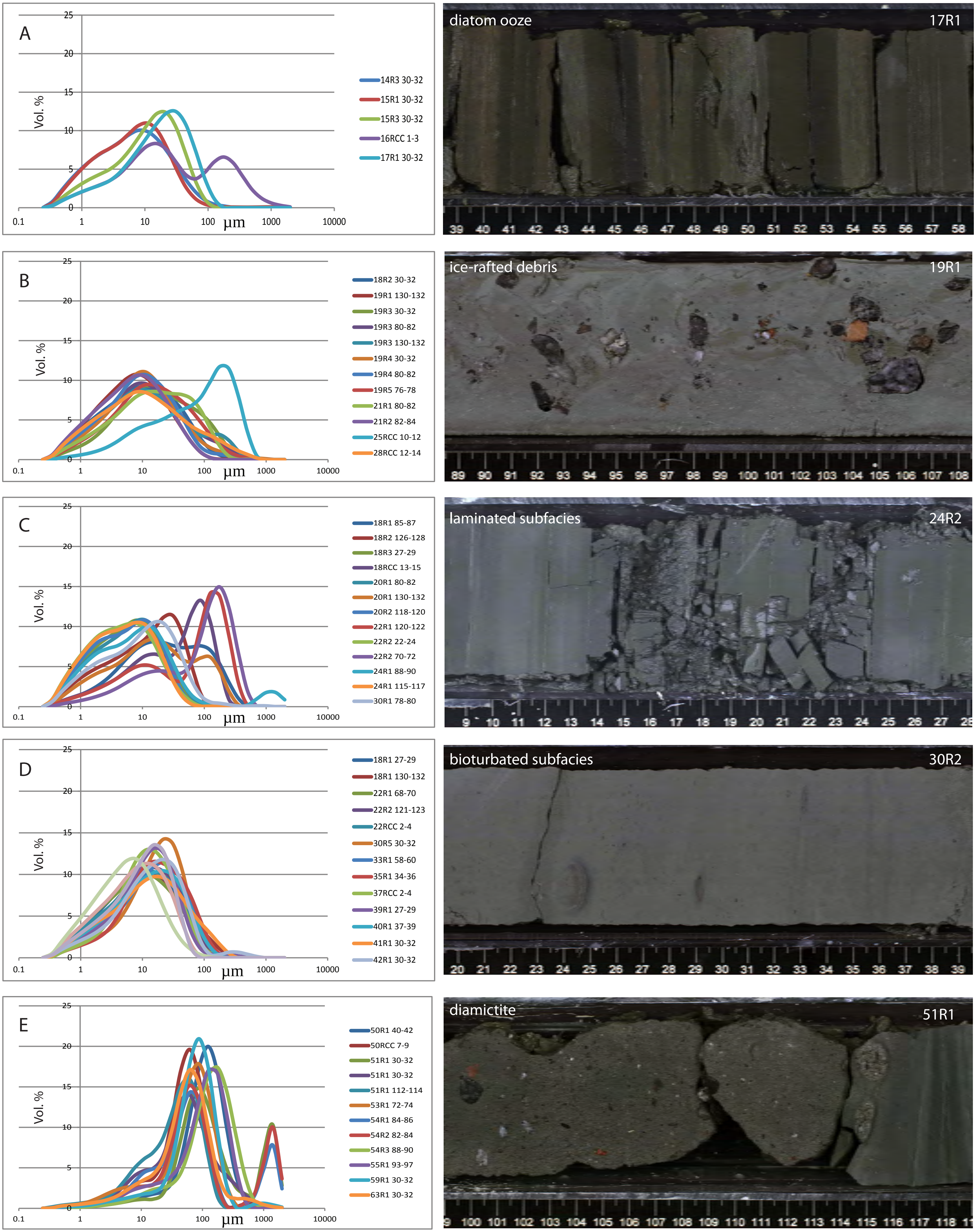

A
Vol. %
μm
0.1
1
10
100
1000
10000
0
5
10
15
20
25
14R3 30-32
15R1 30-32
15R3 30-32
16RCC 1-3
17R1 30-32
diatom ooze
17R1
B
Vol. %
μm
18R2 30-32
19R1 130-132
19R3 30-32
19R3 80-82
19R3 130-132
19R4 30-32
19R4 80-82
19R5 76-78
21R1 80-82
21R2 82-84
25RCC 10-12
28RCC 12-14
ice-rafted debris
19R1
C
Vol. %
μm
18R1 85-87
18R2 126-128
18R3 27-29
18RCC 13-15
20R1 80-82
20R1 130-132
20R2 118-120
22R1 120-122
22R2 22-24
22R2 70-72
24R1 88-90
24R1 115-117
30R1 78-80
laminated subfacies
24R2
D
Vol. %
μm
18R1 27-29
18R1 130-132
22R1 68-70
22R2 121-123
22RCC 2-4
30R5 30-32
33R1 58-60
35R1 34-36
37RCC 2-4
39R1 27-29
40R1 37-39
41R1 30-32
42R1 30-32
bioturbated subfacies
30R2
E
Vol. %
μm
50R1 40-42
50RCC 7-9
51R1 30-32
51R1 30-32
51R1 112-114
53R1 72-74
54R1 84-86
54R2 82-84
54R3 88-90
55R1 93-97
59R1 30-32
63R1 30-32
diamictite
51R1

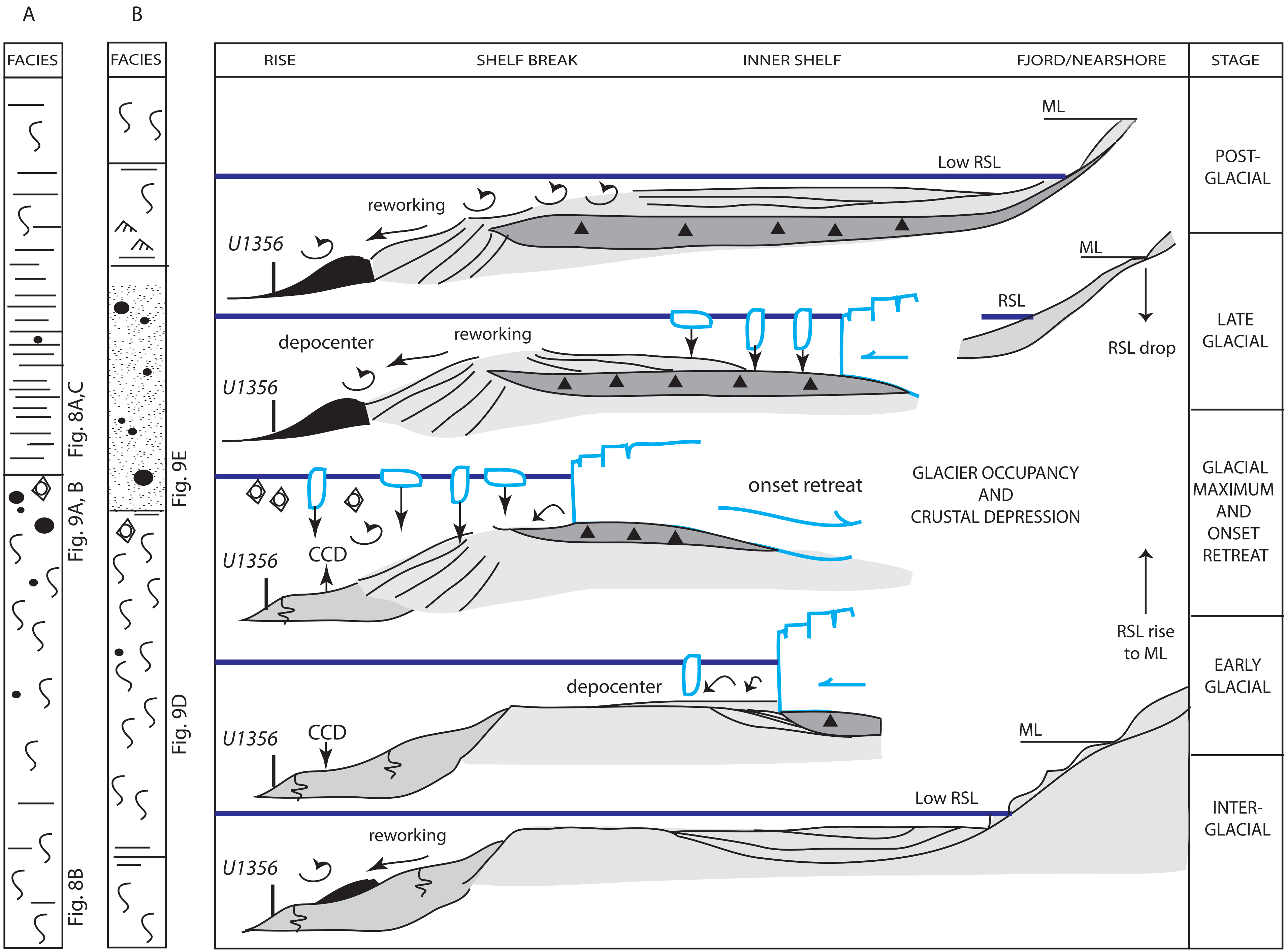
A
B
FACIES
FACIES
RISE
SHELF BREAK
INNER SHELF
FJORD/NEARSHORE
STAGE
ML
Low RSL
POST-GLACIAL
reworking
U1356
ML
RSL
RSL drop
LATE GLACIAL
depocenter
reworking
U1356
GLACIAL MAXIMUM AND ONSET RETREAT
onset retreat
GLACIER OCCUPANCY AND CRUSTAL DEPRESSION
U1356
CCD
RSL rise to ML
EARLY GLACIAL
depocenter
U1356
CCD
ML
Low RSL
INTER-GLACIAL
reworking
U1356
Fig. 8A,C
Fig. 9A, B
Fig. 8B
Fig. 9E
Fig. 9D